MASTER

Scanning tunneling spectroscopy study of the charge transport properties of thin conjugated polymer films

Offermans, P.

Award date:
2001

TU/e technische universiteit eindhoven

Eindhoven University of Technology

Faculty of Applied Physics
Group Semiconductor Physics
Building: N-laag
Postbus 513
5600 MB Eindhoven

Title: Scanning tunneling spectroscopy study of the charge transport properties of thin conjugated polymer films

Author: P. Offermans

Date: June 2001

Graduation report

Daily supervisor : Dr. Ir. M. Kemerink
Supervisor : Dr. P. M. Koenraad

Scanning tunneling spectroscopy study of the charge transport properties of thin conjugated polymer films.

Peter Offermans

14-06-2001

Abstract

We present a study of the charge transport properties of thin conjugated polymer films of MDMO-PPV and P3HT, using a scanning tunneling microscope at room temperature under an inert helium atmosphere. The STM was used to perform several spectroscopic measurements. We find that the tip penetrates the polymer layer when the bias is varied while keeping the feedback loop active. The followed Z(V) trajectory can directly be linked to the internal voltage distribution that is present at the start of the Z(V) measurement. These types of measurements yield information that cannot be obtained by other, non-invasive, techniques. The measurements can be described by a model which treats current injection and space charge limited transport through the bulk on an equal footing. The spread observed in the measured I(V) curves can be explained by variations in barrier height for injection, which can be attributed to the inhomogeneous nature of the polymer/metal interface. I(V) measurements for a tip-sample electrode configuration with bipolar injection, showed a relatively large current at reverse bias, which we attribute to large bandbending near the injecting contact or charge transport through impurity levels. In Z(V) measurements done for a hole-only configuration, wiggles were observed for positive and negative bias, which we attribute to bandbending caused by the buildup of negative induced charges near the positive contact and positive charges near the negative contact. P3HT measurements were performed to investigate the effect of a higher carrier mobility. The P3HT samples were found to be inhomogeneous which is deduced from variations in the mobility over 3 decades.

Contents

Chapter 1

Introduction

Conjugated polymers have attracted widespread attention as promising materials for application in solar cells and organic displays. Also, they have been extensively researched to explain fundamental questions regarding the transport mechanism, the excition binding energy, and the nature of the ground state and the excitations of the polymer. Attention has especially been focused on poly(*p*-phenylene vinylene) (PPV) and its derivatives. Understanding charge transport in PPV-based light emitting diodes has been one of the major goals in the effort to optimize device performance.

In this report, we present a study of the charge transport in thin conjugated polymer films using scanning tunneling spectroscopy at room temperature under an inert helium atmosphere.

In chapter 2 we provide a short introduction to the nature of the charge carriers in conducting polymers. In chapter 3 the experimental setup and the types of measurements are described. A review of existing literature about charge transport in conducting polymers is provided in chapter 4. The model used for describing our measurements in presented in chapter 5. The measurements are discussed in chapter 6.

Chapter 2

Conductivity and luminescence in conjugated polymers

2.1 The origin of the bandgap

The energy gap of a conjugated polymer arises from two sources: a contribution produced by the splitting between bonding and antibonding molecular orbitals of the basic (rigid) structure of the polymer; and a contribution from the interaction of the electrons with a symmetry breaking atomic distortion (Peierls effect) [10]. The bonding (π) and antibonding (π^*) molecular orbitals of the polymer are formed by the overlap of the atomic p_z orbitals at each carbon site, which is called the π system of the polymer. The Peierls effect is responsible for the alternating bond distance between neighbouring carbon atoms in conjugated polymers, which is schematically denoted by alternating single and double bonds in chemical structure diagrams. The difference in energy level of the highest occupied molecular orbital (HOMO) and the lowest unoccupied molecular orbital (LUMO) is the bandgap in conjugated polymers. Inside the bandgap, energy levels can exist which are associated with electronic states of excitations of the polymer chain. These excitations are solitons, polarons, bipolarons and excitons [9].

2.2 Solitons

The most simple conjugated polymer is trans-polyacetylene which is atypical since it has a degenerate ground state which corresponds to two Peierls dimerized configurations, out of phase by one lattice spacing [29], which is shown in figure 2.1.

The degenerate ground state allows to have excitations of the molecule leading from one minimum of the potential to an other minimum of same energy. These excitations are called solitons and correspond to topological kinks that extend several bonds and gradually lead from one conformation to the other conformation, which is shown in figure 2.2.

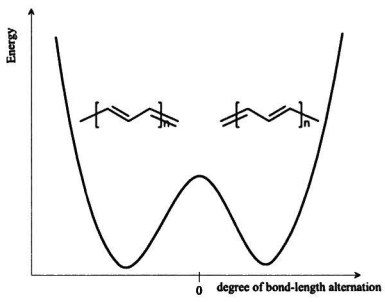

Figure 2.1: Sketch of potential energy curve for trans-polyacetylene showing two energetically equivalent structures.

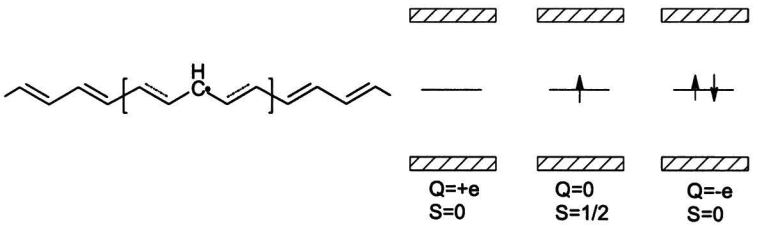

Figure 2.2: Sketch of neutral soliton in trans-polyacetylene. Also shown are the energy level schemes for a postively charged soliton, a neutral solition and a negatively charged soliton.

The precence of the soliton introduces a localized electronic state at midgap. A singly occupied state corresponds to a neutral soliton. A unoccupied or doubly occupied state corresponds to a positive respectively a negative soliton, which is shown on the right side of figure 2.2.

2.3 Polarons

In most polymers isolated solitons do not exist because these molecules do not have a degenerate ground state. In these polymers another type of excitation can exist which is called a polaron. A polaron is a relaxation of the polymer chain which can extend over several units. A polaron can be formed by adding or removing a charge to or from the chain. A hole-polaron is formed by removing an electron from the HOMO. A electron-polaron is formed by adding an electron to the LUMO. In figure 2.3 a hole-polaron is schematically shown for poly(p-phenylene vinylene) (PPV).

As can be seen in the figure, the structure of the aromatic rings in the polymer chain changes from the benzoid structure of the ground state, to a different conformation called the quinoide structure, which is higher in energy, and then again to the benzoide structure. Therefore, one can think of a polaron as a bound charged kink/anti-kink pair. The closer the kink/anti-kink pair comes together the larger the deformation of the chain. Increasing distance between the kink/anti-kink pair means a larger part of the chain has a conformation with higher energy. The presence of polaron introduces two localized electronic states, bonding and anti-bonding, in the gap symmetrically placed about the

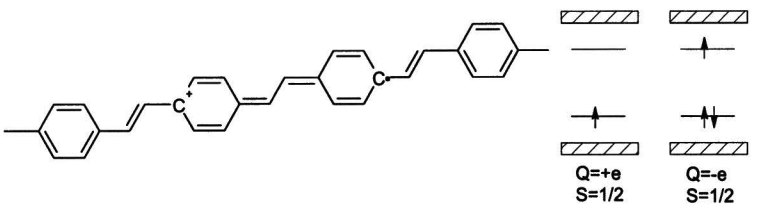

Figure 2.3: Sketch of hole-polaron in PPV. Also shown are the energy level schemes for a postively charged polaron and a negatively charged polaron.

Fermi energy, which is shown on the right side of figure 2.3 .

2.4 Bipolarons

For polymers with a nondegenerate ground state, interaction between polarons leads to the formation of bipolarons. A bipolaron can be thought of as a double charged kink/anti-kink pair. Just like a polaron, a bipolaron has two electronic states in the bandgap. However, because of the stronger deformation of the chain introduced by the bipolaron, the two states are closer to the Fermi level. In figure 2.4 a positively charged bipolaron in poly(p-phenylene vinylene) (PPV) is depicted with the corresponding energy levels. Note that a bipolaron makes spinless conduction possible.

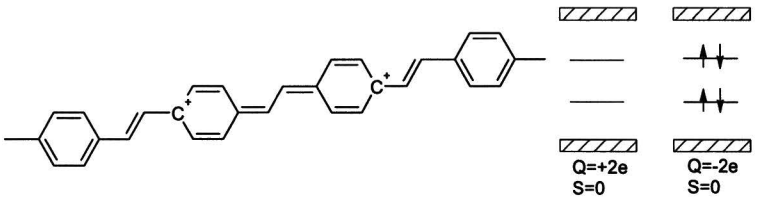

Figure 2.4: Sketch of positively charged bipolaron in PPV. Also shown are the energy level schemes for a postively charged bipolaron and a negatively charged bipolaron.

2.5 Excitons and luminescence

When a hole-polaron and an electron-polaron come in proximity of each other these two polarons can form an exciton-polaron due to Coulomb interaction. An exciton-polaron introduces two singly occupied electronic states in the bandgap. When the spin orientation of these single electron states is anti-parallel, the exciton is in the singlet state S_1. When the spin orientation is parallel, the exciton is in the triplet state T_1 . Figure 2.5 shows the exciton in PPV with the corresponding energy level diagram for a singlet and a triplet exciton.

When the singlet state S_1 of the polaron-exciton decays to the ground state S_0 and a photon is emitted, one speaks of fluorenscence. Another way of radiative decay is phosphorescense which, unlike fluorescence, involves a spin flip $T_1 \rightarrow S_0$. Since this is a forbidden transition, phosphorescence is a very slow

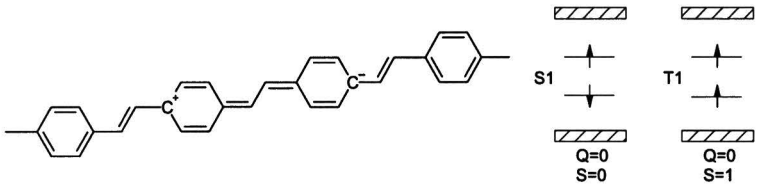

Figure 2.5: Sketch of polaron-exciton in poly(p-phenylene vinylene). Also shown is the energy level scheme for the singlet and triplet state of the exciton.

proces and nonradiative decay will be dominant. Other nonradiative decay processes are intersystem crossing of singlets to a low-lying triplet state or direct nonradiative decay to the ground state creating phonons [3][22]. In figure 2.6 the various ways of decay of an exciton are depicted.

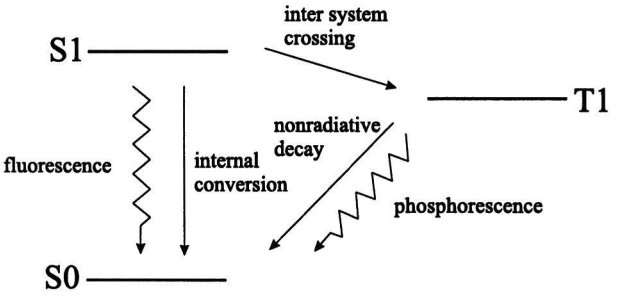

Figure 2.6: Decay mechanisms of the singlet state of the exciton.

Chapter 3

Experimental setup

3.1 Introduction

The experiments were performed using a scanning tunneling microscope at room temperature under an inert helium atmosphere. Figure 3.1 shows a schematic representation of the used setup.

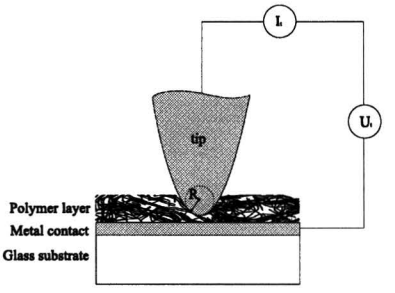

Figure 3.1: Schematic representation of an STM tip on a polymer sample.

The samples are described in section 3.2. Details about sample preparation are provided in section 3.3. The tips are etched from platinum wire in a four step proces, which is described in section 3.4. Four types of measurements were performed using the STM. These types of measurements are described in section 3.5. Section 3.6 deals with the calibration of the STM.

3.2 The samples

Three different sample configurations have been used for the measurements: MDMO-PPV on an Ytterbium lectrode, MDMO-PPV on a Gold electrode and P3HT on a Gold electrode. Glass substrates are used. Samples are provided by Jeroen van Duren. Details about the sample preparation are given in the next section.

MDMO-PPV (poly[2-methoxy,5-(3,7-dimethyl-octyloxy) *p*-phenylene vinylene]) is a conjugated polymer which is used in polymer light emitting devices and solar cells. The thickness of the MDMO-PPV film is estimated to be in the order of 60 nm. AFM measurements on the MDMO-PPV films indicated a RMS-roughness of about 5 nm. We estimated the zero-field mobility of the MDMO-PPV to be in the order of 5e-11 m^2/Vs [25]. The chemical structure of MDMO-PPV is shown on the left of figure 3.2 .

To investigate the effect of a higher carrier mobility, P3HT (poly(3-hexylthienylene)) was used. The mobility of the P3HT was estimated to be at least one decade higher than of PPV [1]. The thickness of the P3HT film is unknown but estimated to be more than 100 nm [1]. Since the P3HT film was known to be inhomogenous, we expected the mobility to vary strongly [1]. We found that, indeed, the mobility varied over 3 orders of magnitude as is discussed in section 6.4. On the right of figure 3.2 the chemical structure of P3HT is depicted.

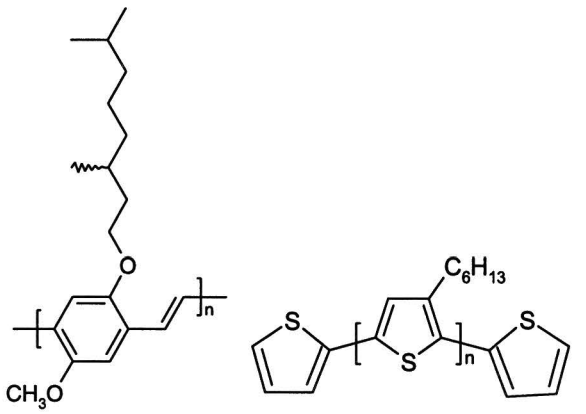

Figure 3.2: Chemical structure of MDMO-PPV (OC_1OC_{10}PPV or poly[2-methoxy,5-(3,7-dimethyl-octyloxy)]PPV) on the left and P3HT (poly(3-hexylthienylene)) on the right.

3.3 Sample preparation

Sample preparation is done in three steps: cleaning of the glass substrate, evaporation of the metal contact on the substrate and finally spincoating of the polymer layer.

Substrate cleaning consists of of the following steps:

1. Ultrasonic cleaning in acetone
2. Rubbing with soap
3. Ultrasonic cleaning in soap ($NaSO_4C_{12}H_{25}$-solution)
4. Washing with demi-water setup

5. Reflux-setup with iso-propanol
6. Drying with nitrogen flow when substrates are still hot
7. UV/Ozone generator treatment

Evaporation of Yb (Au) was done at a deposition rate of 3-4 (0.1-0.7) nm/sec under a pressure of 6e-6 mbar and a sampleholder rotation speed of approximately 1 Hz. Both electrodes have a thickness in the order of 100 nm.

The Yb samples are spincoated at room temperature from a 1.1 mg/ml PPV/ortho-xylene solution. Spin rates are 500 rpm for 7 seconds followed by 1500 rpm for 35 seconds. The PPV/Au samples are spincoated from a hot (60-65°C) 1.0 mg/ml PPV/ortho-xylene solution. Spin rates are 500 rpm for 7 seconds followed by 2000 rpm for 35 seconds. P3HT/Au was spincoated at room temperature from a 1.1 mg/ml P3HT/toluene solution. Spin rates are 500 rpm for 7 seconds followed by 2000 rpm for 35 seconds.

Samples are transported in a dark environment but with exposure to air. Before measurement, the samples are stored in the dark under vacuum. The size of the glass substrates is 30x30 mm. For the measurement smaller pieces are used with a size of about 5x5 mm. To facilitate cleaving, gridlines are scratched on the back of the substrates before sample preparation. The cleaving was done in air with exposure to light. The total time a sample is typically exposed to the combination of air and light before measuring is about 15 minutes. Likely, this causes contamination of the samples with O_2, which could result in an increased concentration of electron traps.

3.4 Tip preparation

Tip preparation was done using the method described in Ref. [19]. The tip is etched in a four-step proces from 0.15 mm diameter platinum wire. SEM images of the finished tip are shown in figure 3.6 at different magnifications. The white box in figure 3.6A indicates the microwire of the tip, which is shown enlarged in figure 3.6B and 3.6C. Figure 3.6D shows the apex of the tip.

1. Coarse electrochemical etching
   The first step in the etching process is coarse electrochemical etching using a fresh $CaCl_2/H_2O$/acetone solution. This solution is prepared by adding 7 g of calcium chloride dihydrate powder to 40 ml of a 1:1 mixture of water and acetone. This results in a solution saturated in acetone with a layer of pure acetone on top. The solution is extracted from below the pure acetone layer. The use of aceton is to control the formation of gas bubbles during the etching proces. To slow down the etching proces, the solution is cooled with liquid nitrogen. The etching itself is done by dipping the wire approximately 1 mm deep in the solution while a 40 Hz ac voltage between the tip and a carbon counter electrode is applied as can been seen in figure 3.3. The first step of the etching proces results in the formation of the microwire. The SEM image in figure 3.7A shows the microwire after the first step of the etching proces. The length of the microwire is in the order of 50 μm. The radius of curvature of the apex is generally less than 1 μm.

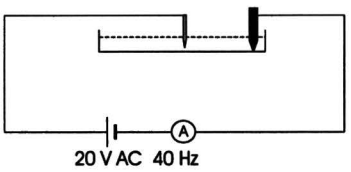

Figure 3.3: Sketch of the electrical circuit used for coarse electrochemical etching.

2. Annealing of the tip
   In the second step, the tip is heated with a Bunsen flame. Only the microwire is held in the flame such that the tip apex glows light orange to yellow. This reduces the amount of dislocations and thus increases the size of the microrcystals in the etched tip. The result of the annealing is shown in figure 3.7B. The radius of curvature has been slightly increased and the surface has become smooth.

3. Micro polishing of the tip
   The third step is micropolishing of the tip in a H_2SO_4/H_2O solution (1:10). The solution is contained in a horizontal glass tube and is in contact with the microwire and the carbon counter electrode. Only the microwire is inserted in the solution which can be observed by a binocular microscope. The carbon counter electrode is grounded and 15 V positive pulses are applied on the tip. The pulses have a duration of 16 μs and a frequency of 4 kHz.The pulses are applied for 10 to 20 seconds. The electrical circuit is shown in figure 3.4. The SEM image in figure 3.7C shows the microwire of the tip after the micro polishing step. The tip has been sharpened and its length has been slightly reduced. The resulting radius of curvature is less than 50 nm.

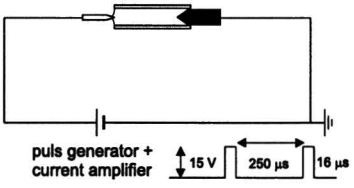

Figure 3.4: Sketch of the electrical circuit used for micropolishing of the tip.

4. Removal of oxide layer
   The last step in the proces of making a tip is to remove the oxide layer which is formed during step 3. A reverse voltage of 1.1 V dc is applied for 90 seconds to the tip while it still is in contact with the H_2SO_4 solution. This step can be stopped when the current has dropped below a few μA. The electrical circuit for the last step is shown in figure 3.5. The SEM image in figure 3.7D shows the microwire of the tip after the last step.

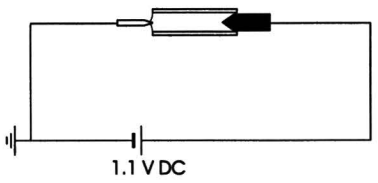

Figure 3.5: Sketch of the electrical circuit used for oxide removal.

3.5 The measurements

An STM measurement begins with moving the tip in the direct neighbourhood of the sample until it makes a tunneling contact with the sample. This is called coarse approach. The width Z of the vacuum gap between tip and sample surface is determined by the required tunneling current I_t and the applied voltage U_t between sample and tip.

After the coarse approach, a topographical image of the sample can be aquired by scanning in the lateral direction over the sample, and adjusting the tip-sample distance using a feedback loop to keep the tunnel current constant. This technique is very sensitive to height variations of the sample surface because of the exponential dependence of the tunnel current on tip-sample distance. The image aquired in this way is called a constant-current image. If the tip-sample distance is kept constant by switching off the feedback loop (or by setting the feedback gain to a small value which is safer), and the current is taken as the variable, a constant-z image is aquired. Generally, two sets of images are aquired: one image composed of line scans taking in the forward scanning direction (left to right), and one in the backward direction (right to left).

It is also possible to define gridpoints on which the STM temporarily stops scanning to perform spectroscopy measurements. In these measurements one variable is changed over a predefined range, and the effect on the remaining variables is measured. In this way three types of measurements have been done:

I-V measurements: the voltage is sweeped over a predefined range, usually starting from the setpoint. The tip-sample distance is kept constant by switching off the feedback loop and the current is measured as a function of voltage.

Z-V measurements: the voltage is sweeped over a predefined range, usually starting from the setpoint. The current is kept constant by keeping the feedback loop active and the tip-sample distance is measured as a function of voltage. The current is monitored as control measurement.

I-Z measurements: the tip-sample distance is varied over a predefined range, not necessarily starting from the setpoint. The voltage is kept constant and the current is measured as function of tip-sample distance.

Z-V and I-Z measurements are usually not performed on hard materials because of the risk of a tip crash. However, on soft materials like disorderd conjugated polymers, the tip can intrude the polymer layer without crashing.

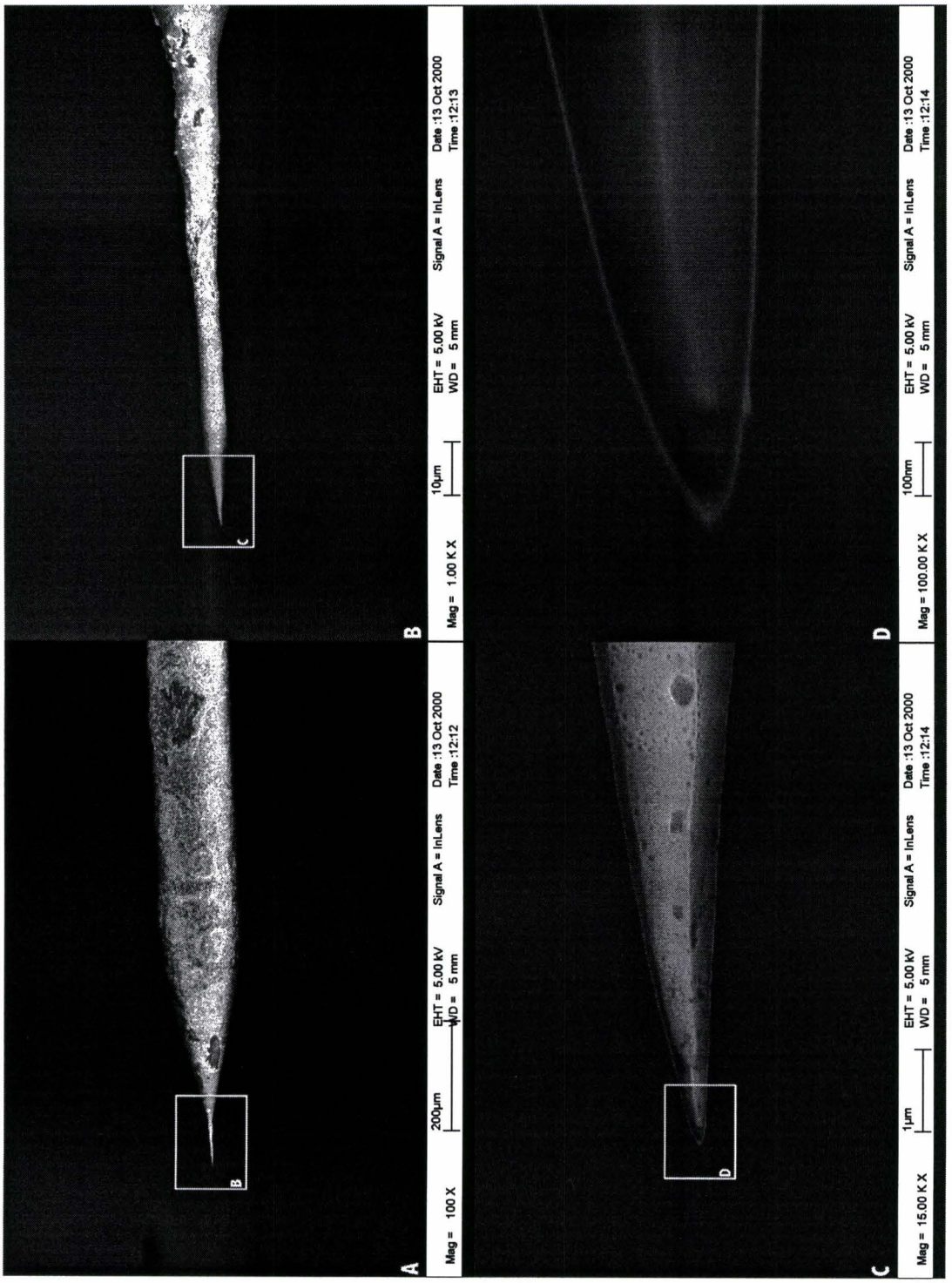

Figure 3.6: SEM images of the etched tip at different magnifications.

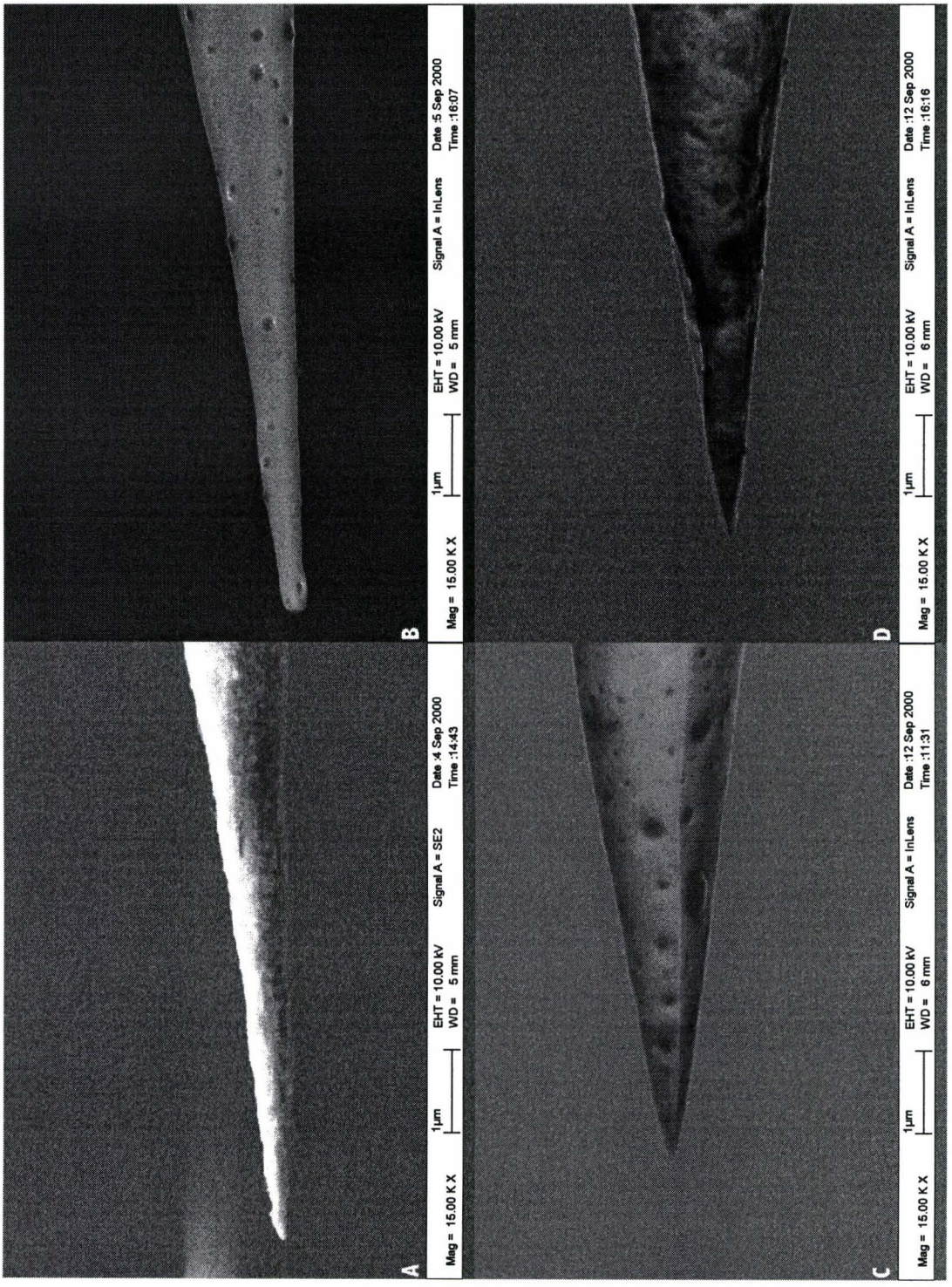

Figure 3.7: SEM images of the microwire of the tip after each step of the etching proces. From A to D the tip is shown after coarse etching, annealing, micro polishing and oxide removal.

3.6 STM calibration

The heart of the STM is a piezoelectric tube scanner. The tube is made of a piezo electric material, which expands or contracts when a voltage is applied to it. To apply a voltage, the tube is metallized on the outer and inner surfaces. The inner metal coating is connected to the z voltage which allows motion in the direction perpendicular to the sample surface. The outside metal coating is sectioned into four quadrants. The four quadrants are connected to a x_1, x_2, y_1 and y_2 voltage which allows bending of the tube in the lateral x and y directions. By continuously changing the voltage to the x and y quadrants, repetitive line scans can be done in forward and backward directions which results in an STM image.

The extent of the displacement of the piezo by applying a voltage on the metallized surfaces is determined by the piezo constants which are defined as:

$$\begin{aligned} K_x &\equiv \tfrac{dx}{dV} &&= \frac{2\sqrt{2}d_{31}L^2}{\pi Dh} \\ K_y &\equiv \tfrac{dy}{dV} &&= \frac{2\sqrt{2}d_{31}L^2}{\pi Dh} \\ K_z &\equiv \tfrac{dz}{dV} &&= \frac{d_{31}L}{h} \end{aligned} \tag{3.1}$$

where L is the length of the piezo tube, D is the diameter of the tube and h the wall tickness of the tube. The quantity d_{31} is the piezo electric constant and can be termined by a so called Chen test [7]. The electric circuit diagram for a Chen test is depicted in figure 3.8.

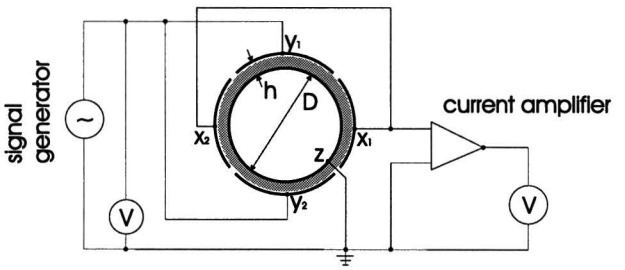

Figure 3.8: Measuring circuit for the double piezoelectric response of a tube scanner.

As can be seen in the figure, the two y quadrants of the tube scanner are connected to a sinusoidal signal from a signal generator. The rms voltage of the sinusoidal signal is measured by an ac voltmeter. The two x quadrants are connected to the ground through the input of a lock-in amplifier used as current amplifier. The stress generated in the x quadrants of the piezoelectric ceramics by applying a voltage on the y quadrants is given by:

$$\sigma_3 = Y\frac{d_{31}VY}{2h},$$

where Y is Young's modulus of the piezoelectric ceramics in the lateral direction under constant electric field and V the applied voltage. The stress in the x

quadrants generates a polarization $P = d_{31}\sigma_3$. The total surface charge on one of the two x quadrants is then:

$$Q = \frac{\pi D L d_{31}^2 V Y}{8h},$$

where D is the diameter and L the length of the piezo tube. By connecting that x quadrant to the ground an ac current is generated:

$$I = \frac{dQ}{dt} = \frac{\pi^2 D L d_{31}^2 Y}{4h} V_0 \cos 2\pi f t.$$

If both x quadrants are connected together the rms value of the current is:

$$\overline{I} = \frac{\pi^2 f D L d_{31}^2 Y}{2h} \overline{V}.$$

In this equation the variables D, h, L and Y are known variables, the current is measured, and V and f are experimental parameters, which results in the determination of d_{31}. This value can be used to calculate the piezo electric constants K_x, K_y and K_z using equation 3.1.

Chapter 4

Theory

Several models exist in literature to describe the conduction proces in conjugated polymers. It has been proposed by Parker [27] that the current-density - voltage (J-V) characteristics of polymer LEDs are controlled by charge injection. At high electric fields (>5e7 V/m) the J-V characteristics are determined by Fowler-Nordheim tunneling (FN) of both electrons and holes through contact barriers arising from the band offset between the polymer and the electrodes. The functional form for FN-tunneling is

$$J = J_0(E/E_0)^2 \exp(-E_0/E). \tag{4.1}$$

If there is a significant difference in the barrier height to injection, the smaller of the two barriers controls the (J-V) characteristics, while the larger of the two barriers determines the device efficiency. If the barriers for injection into the LUMO (HOMO) level are smaller than the barriers for injection into the HOMO (LUMO) level of the polymer, the device is called an electron-only (hole-only) device, see figure 4.1.

There are several problems with this model. Quantitatively, at these high fields the predicted Fowler-Nordheim currents exceed the experimentally observed currents by several orders of magnitude. Furthermore, at low fields the tunneling model was found not to be applicable to the experimental J-V characteristics as is indicated by a deviation from a straight line in a Fowler-Nordheim plot. (A Fowler-Nordheim plot is a plot of $\ln(J/E^2)$ against $1/E$.) This deviation has been attributed to the contribution of thermionic emission to the current [29], and to band bending effects at the interface [6].

Thermionic emission is the classical way by which an electron can thermally surmount a potential barrier and is given by [32]:

$$J = AT^2 \exp(-\phi_b/k_BT) \tag{4.2}$$

where $A = \frac{qm_e k_B^2}{2\pi^2\hbar^3}$ is the Richardson constant , T is the temperature, k_B Boltzmann's constant and ϕ_b the barrier height.

In undoped polymers band bending by Schottky barrier formation is believed not to occur because of the lack of free charge carriers. However, it was proposed in [6] that charge transfer at the metal/polymer interface can result in the formation of a bipolaron lattice at the interface. The bipolaron lattice is then responsible for band bending at the interface. When the externally applied field

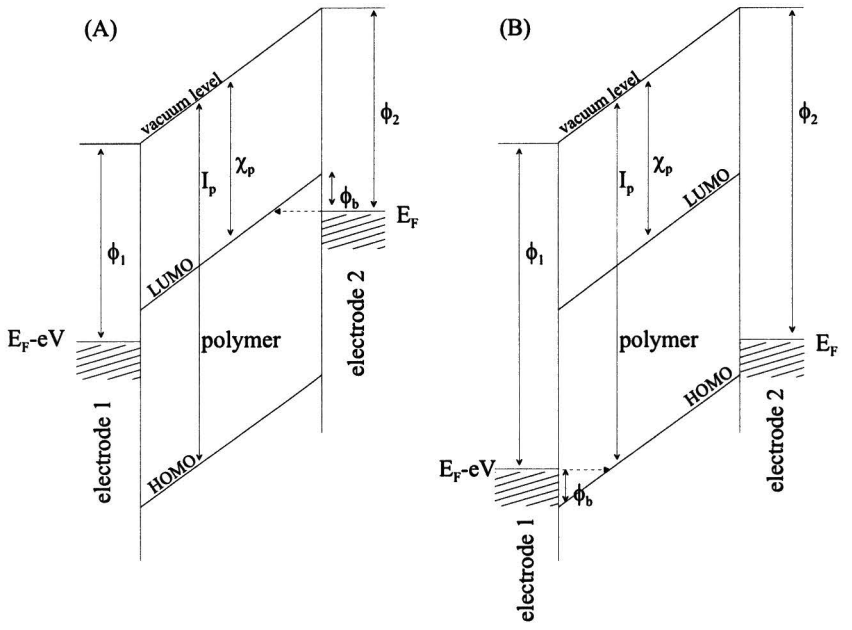

Figure 4.1: Energy level diagram showing an electron-only device (A) and a hole-only device (B) with Fowler-Nordheim tunneling into polymer bands through a triangular barrier ϕ_b arising from the band offset between the polymer bands and the electrodes. Indicated in the figure are the Fermi energy E_F, the ionization potential of the polymer I_p, the electron affinity of the polymer χ_p, and electrode workfunctions ϕ_1 and ϕ_2.

is significantly larger than the field change near the contact caused by the band bending, a model which assumes tunneling through a triangular barrier at the interface will predict the correct field dependence of the current. However, in the low field regime the measured current will differ considerably from the predicted current which then could explain the deviations in a Fowler-Nordheim plot at low fields.

Another possible explanation for this deviation was proposed in [20]. Here the claim was made that the approximation of the Fermi-Dirac distribution by a step function in Fowler-Nordheim theory is responsible for the deviation from a straight line in a Fowler-Nordheim plot.

The overestimation of the current by many orders of magnitude by Fowler-Nordheim theory has been contributed [12] to the low mobility of organic materials, which results in a large backflow of injected carriers into the injecting contact. The backflow current or interface recombination is the reversed process of thermionic emission and is proportional to the carrier density which is build up near the injecting contact.

When the device quality became higher, an alternative approach was proposed to model polymer devices. In this approach the contact was assumed to be ohmic, i.e. the injection process is ignored, and the low mobility of the material is viewed as the current-limiting factor. In [25] Blom provides a consistent description of the J-V characteristics of PPV devices based on bulk transport through the polymer layer as described by [21] for a single carrier device. The

model of bulk transport assumes that the device current is limited by the space charge inside the bulk of the polymer layer. The distribution of space charge inside the polymer layer is governed by Poisson's equation, and the device current is constant across the polymer layer and carried by the mobile injected carriers only:

$$\begin{cases} J &= e\,\mu(E)\,n_i(x)\,E(x) \\ \frac{\varepsilon}{e}\frac{dE}{dx} &= n_i(x) + n_{ti}(x) \end{cases} \tag{4.3}$$

where $n_i(x)$ is the number of mobile injected carriers, $n_{ti}(x)$ is the number of trapped injected carriers, $\mu(E)$ is a field dependent mobility and ε the dielectric constant of the polymer. The contribution of diffusion current is assumed to be neglible in the bulk and only plays a role in the immediate neighbourhood of the contact [13].

If trapping of carriers is absent and the mobility is taken as consant these equations can be solved analytically resulting in the so-called trap-free square law [21]:

$$J = \frac{9}{8}\varepsilon\mu\frac{V^2}{L^3} \tag{4.4}$$

where L is the thickness of the polymer layer. The trap-free square law has been applied by Blom for hole-only devices [25] and was found to be applicable for devices with low injection barriers. At high electric fields however it was observed that the experimental current density was larger than expected from the trap-free square law. This was explained by a field dependence of the mobility which is attributed to fluctuations in conjugation lengths (energetic disorder), or disorder in the positions and local orientations of the polymer chain (structural disorder) [24]. It was shown that the mobility could be described by Gill's empirical relation

$$\begin{aligned} \mu(E) &= \mu(0)\exp(\gamma\sqrt{E}) \quad \text{with} \\ \gamma &= B\left(\frac{1}{k_BT} - \frac{1}{k_BT_0}\right) \quad \text{and} \\ \mu(0) &= \mu_0\exp(-\frac{\Delta}{k_BT}) \end{aligned} \tag{4.5}$$

which is a particular form of the universal Poole-Frenkel behavior

$$\mu = \mu_0\exp(-\frac{\Theta}{k_BT})\exp(\gamma\sqrt{E}).$$

where the activation energy Θ is a function of temperature and γ the Poole-Frenkel factor.

Because Gill's relation lacks theoretical justification, other expressions for the mobility were proposed, based on Monte-Carlo simulations of transport of carriers in an array of sites exhibiting a Gaussian density of states (hopping) [14]. These (correlated [8]) Gaussian disorder models have similar field dependences of the mobility as equation 4.5. Recently, a different field dependence of the mobility was proposed in [15], based on hopping sites with a square trapping potential, with the following functional form:

$$\mu(E) \sim \sinh(E)/E.$$

This type of mobility dependence was used to explain measurements on undoped samples in which a sharp increase of current with voltage at high fields was observed. The authors obtained the $\exp(\sqrt{E})$ dependence of the mobility for a Coulomb-type trapping potential.

The transport properties of electron-only devices have been explained in [25] by space charge limited conduction with an exponential energy distribution of trap levels. The occurrence of an abrupt increase of the current at a certain critical voltage is characteristic for an insulator with traps [21]. For trap levels located at a single energy level this is an extremely sharp transition at which the current directly switches from Ohmic conduction carried by free intrinsic carriers, to space charge limited conduction. This transition is called the trap-filled limit because all traps are filled instantly during this transition. A more gradual increase can be described by an exponential distribution of trap levels:

$$N_t(E) = \frac{N_t}{k_B T_t} \exp\left(\frac{E - E_c}{k_B T_t}\right) \tag{4.6}$$

with $N_t(E)$ the trap density of states at energy E , N_t the total density of traps, $k_B T_t$ the width of the distribution and E_c the conduction band energy. The concentration of trapped injected carriers at position x can be found by integrating equation 4.6 from the thermal position of the Fermi-level F_0 at zero current to the quasi Fermi-level $F(x)$ at position x:

$$n_{ti}(x) = \int_{F_0}^{F(x)} N_t(E)\, dE \tag{4.7}$$

which can be expressed in terms of $n_i(x)$ using

$$n_i(x) = N_c \exp\left(\frac{F(x) - E_c}{k_B T}\right)$$

where N_c is the density of states of the conduction band. Equation 4.3 together with equation 4.7 has been solved by [21] under the assumption that $n_{ti}(x) \gg n_i(x)$ and results in the following current-voltage relation:

$$J = K \frac{V^{(m+1)}}{L^{(2m+1)}} \tag{4.8}$$

with

$$K = N_c \mu \exp(1-m) \left[\frac{\varepsilon m}{N_t(m+1)}\right]^m \left(\frac{2m+1}{m+1}\right)^{m+1} \text{ and } m = T_t/T \ .$$

In [5] space charge limited conduction with an exponential trap distribution was found to be in very good agreement with measured J-V characteristics for ITO/PPV/Al devices. However, the observed thickness dependence of ITO/PPV/Au devices could not be explained, and the experimental variation of m with temperature showed that the steepness T_t of the trap distribution decreased with decreasing temperature. This was explained by proposing that the trap distribution is not truly exponential, but a much steeper function of energy closer to the HOMO levels [4]. A further problem with this model is the unphysical picture of a single transport state and the assumption of a field and temperature independent mobility, which is not consistent with an energetically disorderd system. The assumption of a single transport state results in

a relationship between the the mobile injected carriers n_i the trapped injected carriers n_{ti} of the form:

$$n_i = \Theta\, n_{ti}^m \quad \text{with } \Theta = N_c\, N_t^{-m}.$$

It was shown that a Gaussion transport state distribution could result in a similar relationship between the free and trapped carriers, which could also explain the experimental variation of m with temperature. To get a consistent picture with a hopping type conduction for disorderd molecular systems, it was proposed that the observed trap distribution is just the tail of Gaussion LUMO and HOMO density of states through which hopping occurs as is shown in figure 4.2.

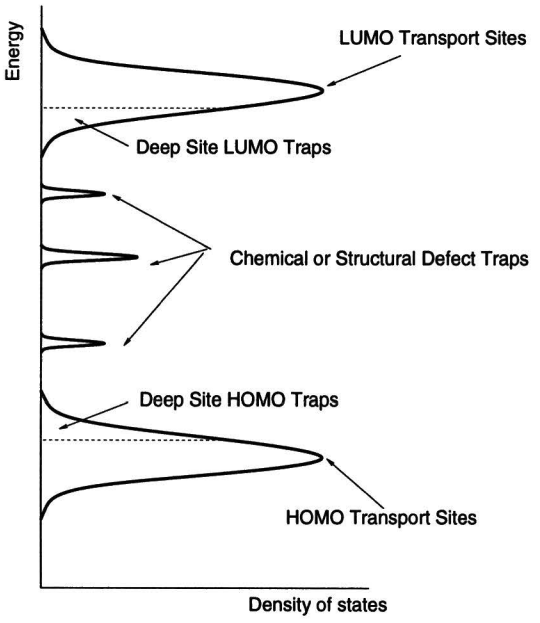

Figure 4.2: Complete picture of the deep states trapping model. The HOMO and LUMO states form Gaussian DOS distributions on either side of the carrier energy gap. The more numerous subgap states act as transport states. The deep tail states act as continuous, pseudoexponential trap distributions. Chemical impurities or structural defects form relatively discrete, isoelectronic trapping levels in the energy gap.

In [18] a simple model is presented to reconcile the discrepancies between models with a field-dependent mobility, and models which assume the presence of traps and a single conduction state. In this model, states are not artificially devided into conducting states and trap states. Using a thermal activated mobility function $\mu(E) = \mu_0 \exp(E/k_BT)$ and a exponential density of states $D(E) = \frac{N}{\sigma} \exp(-\frac{|E|}{\sigma})$, a current-voltage relationship was derived with a similar form as equation4.8, with $m = \sigma/k_BT$.

To describe the observed bulk conduction which is dominant for low barriers ($\phi_b <$ 0.3 eV) as well as the current injection process, which is dominant for higher barriers ($\phi_b >$ 0.4 eV), a model was proposed by Davids *et al.* [12] which combines both mechanisms including recombination and carrier generation. In

this model, the transport of electrons and holes in the polymer layer is described by time dependent continuity equations, with a drift-diffusion form for current density, coupled to Poisson's equation:

$$\begin{aligned} \frac{\partial n}{\partial t} - \frac{1}{e}\frac{\partial J_n}{\partial x} &= G - R \\ \frac{\partial p}{\partial t} - \frac{1}{e}\frac{\partial J_p}{\partial x} &= G - R \\ \frac{\partial E}{\partial x} &= \frac{e}{\varepsilon}(p - n) \end{aligned}$$

where

$$J_n = e\mu_n \left(nE + \frac{k_B T}{e}\frac{\partial n}{\partial x} \right)$$

$$J_p = e\mu_p \left(pE - \frac{k_B T}{e}\frac{\partial p}{\partial x} \right).$$

Here, n (p) is the electron (hole) density, J_n (J_p) is the electron (hole) current density, G (R) is the carrier generation (recombination) rate, μ_n (μ_p) is the electron (hole) mobility. The recombination is bimolecular $R = \gamma np$, where the recombination coefficient is of the Langevin type given by $\gamma = e\mu_m/\varepsilon$, where μ_m is the larger of μ_n and μ_p. The generation rate is determined from the recombination rate using detailed balancing, $G = \gamma n_e p_e$, where $n_e p_e$ is the product of electron and hole equilibrium densities:

$$\begin{aligned} n_e &= N_{DOS} \exp - \frac{(E_c - E_F - e\,\phi(x))}{k_B T} \\ p_e &= N_{DOS} \exp \frac{(E_v - E_F - e\,\phi(x))}{k_B T} \end{aligned}$$

where N_{DOS} is the density of conjugated chain segments times the number of ways that a chain segment can be occupied by and electron or hole, E_F is the Fermi energy, $\phi(x)$ is the electrostatic potential at position x, and E_c and E_v are the conduction band (LUMO) resp. valence band energies (HOMO). Boundary conditions are given by specifiying the currents at the boundaries $x = 0$ and $x = L$ where L is the thickness of the polymer layer.

The total device current was assumed to consist of three components: tunneling current, thermionic emission, and a backflowing interface recombination, which is the reversed proces of thermionic emission. Image force lowering of the barrier height for tunneling and thermionic emission is also included in the model. The mobility was taken of the form $\mu = \mu_0 \exp(\sqrt{E/E_0})$. It was shown that for low injection barriers the current flow is space charge limited and the electric field across the structure highly nonuniform. For higher injection barriers the current flow was shown to be injection limited with a nearly uniform field distribution. At small bias in the injection limited regime (i.e. for high barriers), thermionic emission was shown to be the dominant injection mechanism and the combination of thermionic emission and interface recombination determine the net device current, which is much smaller than both the thermionic emission

and interface recombination current, since they nearly cancel. At higher bias the net device current was shown to be determined by the combination of tunneling injection current and interface recombination.

In [16] a simplified model was proposed based on the model by Davids *et al.* [12]. In this model only single carrier devices are considered and both time dependence and diffusion is neglected:

$$\frac{dJ}{dx} = 0 \tag{4.9}$$

$$\frac{\varepsilon}{e}\frac{dE}{dx} = p \tag{4.10}$$

$$J = e\mu(E,T)pE \tag{4.11}$$

The temperature dependence is accounted for both in the injection terms (the thermionic emission and interface recombination current) and in the transport (through the mobility using equation 4.5). The model was found to be in agreement with measurements over a temperature range from 100 to 300 K. The barrier height to injection for an ITO/MEH-PPV/Al device was found to have a functional dependence on temperature similar to the shift of the absorption of the polymer [17].

Chapter 5

The model

In this chapter the model used in this work is discussed. The model is similar to the model discussed in [16]. The model is based on the requirement that the current, potential and electric field are continuous across the polymer layer. To satisfy continuity of the current, the injection current has to be equal to the bulk current. To satisfy continuity of the electric field and potential, the electric field at the injecting contact is used as a boundary condition for the electric field distribution across the polymer layer. In section 5.1 the injection current is discussed. In section 5.2 the bulk conduction is discussed, and in section 5.3 the calculation of IV, IZ and ZV curves is described. In section 5.4 the model is compared to existing literature.

5.1 Injection

The injection current J_D is composed of three terms: tunneling current, thermionic emission and interface recombination, which are shown schematically in figure 5.1:

$$J_D = J_{TUN} + J_{TH} - J_{IR} \tag{5.1}$$

The tunneling current is calculated using a modified Fowler-Nordheim expression including the image force [12]:

$$J_{TUN} = \frac{C}{\phi_b}\left(\frac{E}{t(y)}\right)^2 \exp\left(\frac{-v(y)B{\phi_b}^{3/2}}{E}\right) \tag{5.2}$$

where

$$C = \frac{2.2e^3}{8\pi h}$$

$$B = \frac{8\pi\sqrt{2m}}{2.96he}$$

$$v(y) = \sqrt{1+y}\left[E\left(\sqrt{\frac{1-y}{1+y}}\right) - yK\left(\sqrt{\frac{1-y}{1+y}}\right)\right]$$

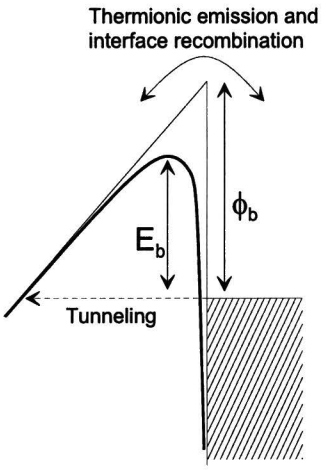

Figure 5.1: Schematic representation of an injection barrier. The barrier heigth is effectively lowered by the image force. The arrows indicate the tunneling current, thermionic emission and interface recombination.

$$t(y) = \frac{1}{\sqrt{1+y}} \left[(1+y)\, E\left(\sqrt{\frac{1-y}{1+y}}\right) - y\, K\left(\sqrt{\frac{1-y}{1+y}}\right) \right]$$

$$y = \frac{e\sqrt{\frac{eE}{4\pi\varepsilon}}}{\phi_b}$$

where $E(z)$ and $K(z)$ are complete elliptic integrals of the first and second kind, see appendix. The prefactors C and B are derived in [31].

The thermionic emission current J_{TH} is given by [32]:

$$J_{TH} = AT^2 \exp(-E_b/k_B T)$$

where A is the Richardson constant as in equation 4.2. E_b is the interfacial energy barrier. Because of the image force, E_b depends on the electric field $E(0)$ at the interface :

$$E_b = \phi_b - e\sqrt{\frac{eE(0)}{4\pi\varepsilon}}. \tag{5.3}$$

The interface recombination current J_{IR} is proportional to the carrier density at the interface:

$$J_{IR} = \nu p(0)$$

The proportionality constant ν is determined by detailed balance of equation 5.1 at zero bias where J_{FN} and J_D vanish (see appendix):

$$\nu = \frac{AT^2}{N_{DOS}}$$

where N_{DOS} is the density of conjugated chain segments times the number of ways that a chain segment can be occupied by an electron or hole. The carrier

density at the interface $p(0)$ is determined by substituting the expression for the space charge limited current

$$\begin{aligned} J_D &= e\,\mu(E(0))\,p(0) \quad \text{with} \\ \mu(E(0)) &= \mu(0)\exp(\gamma\sqrt{E(0)})\,E(0) \end{aligned} \tag{5.4}$$

into equation 5.1, which results in:

$$p(0) = \frac{J_{TH} + J_{TUN}}{\nu + e\mu(E(0))\,E}$$

Note, that the use of a Fowler-Nordheim expression for the tunneling current and equation 5.3 for barrier lowering, a triangular injection barrier is assumed. This is correct only if there are no bandbending effects near the interface.

We apply equation 5.1 to a configuration in which one electrode is replaced by the STM tip, as is shown in figure 5.2. This enables us to vary the distance between both electrodes, by using the STM tip as an intrusive probe.

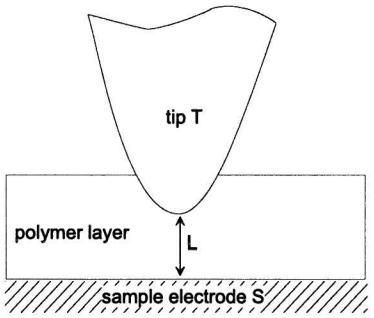

Figure 5.2: Schematic representation of the tip/polymer/sample-electrode setup using the tip as an intrusive probe.

If the tip-sample distance L is small enough for direct tunneling to the bottom electrode, the Fowler-Nordheim expression for the tunneling current is not applicable anymore. In this case a general expression for the tunneling current is used as is described by Feenstra [28]:

$$J = \frac{m_e e}{2\pi^2\hbar^3}\int_{E_F-eV}^{E_F}\int_{E(1-\alpha)+\alpha(E_F-eV)}^{E} D(W)\,dW\,dE \tag{5.5}$$

where $\alpha = m^*/m_e$ and the transmission coefficient $D(W)$ is evaluated in the WKB approximation:

$$D(W) = \exp\left(-2\sqrt{2m^*}/\hbar\int_{z1}^{z2}\sqrt{V(z)-W}dz\right).$$

The potential $V(z)$ is taken to be the sum of a trapezoidal barrier plus a classical image force given by:

$$\begin{aligned} V(z) &= (E_F - eV + \phi_s)(1-\frac{z}{L}) + (E_F + \phi_t)(\frac{z}{L}) + V_{img}(z) \\ V_{img}(z) &= -\frac{e^2}{16\pi\varepsilon}\frac{L}{z(L-z)} \end{aligned}$$

where ϕ_S and ϕ_T are the barrier heights for injection from the bottom electrode (S) respectively the tip (T), see figure 5.4. Note that Simmons [31] uses an image force which is a factor $2 \times 1.15 \ln(2)$ larger. Feenstra [28] uses half of this. In the limit where the tip-bottom electrode distance $L \gg z$ our relation results in the expression of the image force given by Sze [32].

Equation 5.5 is evaluated using the identity given by [28]:

$$\int_{E1}^{E2} dE \int_{aE+b}^{E} D(W)dW = \int_{aE_2+b}^{E_2} D(W)(E_2 - W)dW$$
$$- \int_{aE_1+b}^{E_1} D(W)(E_1 - W)dW + \frac{1}{a}\int_{aE_1+b}^{aE_2+b} D(W)[W - (aW + b)]dW.$$

5.2 Bulk conduction

The field distribution across the polymer layer is calculated by solving the set of equations 4.3 for the trap-free case. This is done by substituting Poisson's equation for the carrier density in the expression for the space charge limited current, which results in a first order differential equation for the field:

$$\frac{dE}{dx} = \frac{J_D}{\varepsilon\mu(0)\exp(\gamma\sqrt{E})\,E} \tag{5.6}$$

This first order differential equation is solved using a variable step sized Runge-Kutta method, with boundary condition $E = E(0)$. The potential at $x = L$ is found by integration of the electric field:

$$V = \int_0^D E(x)\,dx + V_{bi} + \phi_b \tag{5.7}$$

where ϕ_b is barrier height for injection and V_{bi} the built-in voltage and D is the width of the region in which space charge limited conduction takes place, which is the thickness of the polymer layer minus the tunneling distance into the polymer layer.

In the one-dimensional approximation, the total tunneling current is $I = AJ$, where A is the tip area and J the current density. To verify if the one-dimensional equations used for space charge limited conduction are applicable to the tip/polymer/electrode configuration used in this work, the current density distribution across the surface of the tip was determined by applying the one-dimensional equations to a set of field lines originating from the tip. The field lines are approximated by circle segments perpendicular to the tip and the bottom electrode. The strength of the field at the tip surface was taken to be zero. The shape of the tip is approximated by a parabola with radius of curvature R . This is shown in figure 5.3. Parameters used in the calculation are $\mu(0)$ = 5e-11 m^2/Vs, γ = 5.4e-4 $(m/V)^{1/2}$, N_{DOS} =1e27 m^{-3} and V = 10 V. From this figure it can be concluded that the effective surface A of the tip can be approximated by $A = \pi(R/3)^2$. Note that the exact value of A is not significant since it can be discounted in the other variables.

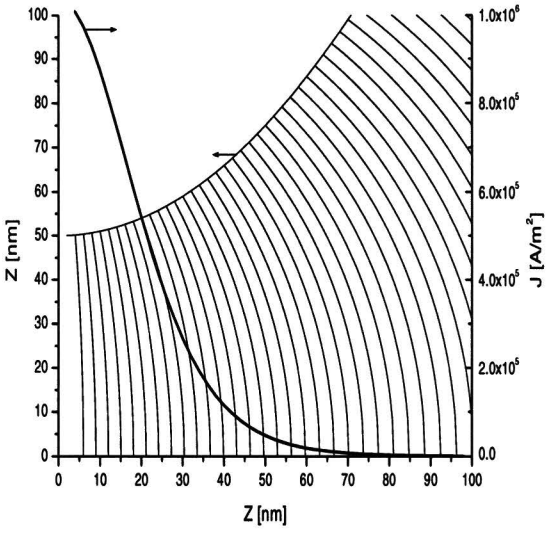

Figure 5.3: Calculated current-density profile as function of x-coordinate across the surface of the tip. Field lines are approximated by circle segments perpendicular to tip and bottom electrode. The radius of curvature of tip used in the calculation is 50 nm, the tip-electrode distance is 50 nm. The strength of the field at the tip surface is taken to be zero. Parameters used in the calculation are $\mu(0)$ = 5e-11 m^2/Vs, γ = 5.4e-4 $(m/V)^{1/2}$, N_{DOS} =1e27 m^{-3} and V = 10 V.

5.3 Calculation of IV, IZ and ZV curves

Calculation of IV curves is done by taking the current as a fixed variable for each point on the curve, and calculating the corresponding voltage by integration of the field across the polymer layer using equation 5.7. The field distribution across the polymer layer is calculated using equation 5.6, which needs a boundary condition. This boundary condition is provided by the electric field $E(0)$ at the injecting contact. Since the injection current depends on the strength of the electric field at the injecting contact via both the tunneling current J_{TUN} and the thermionic emission J_{TH}, the electric field $E(0)$ can be determined implicitly by requiring a certain injection current J_D, which is equal to the specified bulk current. Calculation of IZ curves is done similar to the calculation of IV curves, except that the distance Z between tip and bottom electrode is implicitly determined by integration of the electric field using a fixed tip-sample voltage V.

For IV and IZ curves, the tunneling distance z_{FN} into the polymer is calculated by $z_{FN} = \phi_b/E(0)$, where ϕ_b is the injection barrier. This assumes a triangular tunneling barrier, which is not necessarely true for small tip-sample distances and voltages, as is discussed in section 5.1. The combination of small tip-sample distance and voltage occurs in the case of ZV measurements. Figure 5.4 shows the proposed band diagram at different voltages during a ZV measurement for a hole-dominated device with unequal barrier heights. For simplicity,

the effect of the image force is not shown in the figure.

If the applied voltage equals $V = 0$ then no current will flow, and the field between the contacts is constant and equal to the internal built-in field, given by $E_{int} = (\phi_S - \phi_T)/Z$, where ϕ_S is the barrier height for hole injection at the electrode/polymer interface, ϕ_T the barrier height for hole injection at the tip/polymer interface. If the applied sample voltage $V > 0$ then a tunneling current can flow between the contact, through a trapezium shaped barrier, which is described by equation 5.5. As soon as the applied voltage is larger than the built-in voltage $V_{bi} = \phi_S - \phi_T$, thermionic emission and interface recombination are possible because the field has the right sign. When the applied voltage is equal to $V = \phi_S$ then tunneling occurs through a triangular barrier, which is described by the Fowler-Nordheim expression. Increasing the voltage beyond $V = \phi_S$ results in bandbending which is described by space charge limited conduction. To satisfy continuity of the current, it is required that the triangular injection barrier remains the same while the voltage is further increased. Since the field distribution across the polymer layer is entirely determined by $E(0)$ and the specified current, it follows that field distribution does not change with voltage. Therefore, a ZV measurement gives explicit information about the potential distribution $V(z)$ across the polymer layer.

The contribution to the total current by the electrons is neglected in this model, because of the assumption that the hole mobility is larger than the electron mobility [25], and the barrier for injection for holes is smaller than the barrier for injection of electrons making the holes the majority carrier [27].

5.4 Discussion of the model

In order to test the model, the current density as a function of applied voltage is calculated using parameters as used by [16]. Figure 5.5 shows the result for a 120 nm sample with N_{DOS} = 1e27 m^{-3}, γ = 3.2e-4 $(m/V)^{1/2}$, $\mu(0)$ = 1.7e-11 m^2/Vs, T = 295 K, $\varepsilon = 3\varepsilon_0$ and varying barrier heights for injection ϕ_b = 0.1, 0.2, 0.3, 0.4, 0.5 and 0.6 eV. The dashed lines are calculated as done by [16], i.e. neglecting the tunneling distance in the polymer and integrating the electric field across the entire polymer layer, starting at the injecting contact. The solid lines are calculated using equation 5.7, with equation 5.5 used for the tunneling current component. The solid lines start to deviate significantly from the dashed lines for barrier heights smaller than 0.3 to 0.4 eV. At these low barrier heights, the tunneling distance into the polymer becomes increasingly large, reducing the distance over which space charge limited conduction takes place. This results in higher currents at low voltages. It is questionable if the assumption of a triangular tunneling barrier still holds at low barrier heights, since the injection switches to Ohmic behavior at low barrier height, and the current flow is dominated by space charge limited conduction. This also explains why a model which entirely neglects the injection current [26], gives good results for contacts with low barriers to injection. For barrier heights larger than 0.4 eV, the current flow is injection limited and the assumption of a triangular tunneling barrier is valid, since for these barrier heights the electric field is almost constant, which results in straight bands [23].

As noted above, the solid lines in figure 5.5 are calculated using equation 5.5 for the tunneling current. In figure 5.6 the same calculation is shown using the Fowler-Nordheim expression for the tunneling current. Barrier heights used are 0.3, 0.4, 0.5 and 0.6 eV. As can be seen in the figure, there is some deviation at low voltages for a barrier height of 0.3 eV. For smaller barrier heights the calculation done using the Fowler-Nordheim expression leads to unacceptable results. For barrier heights larger than 0.3 eV, the calculation leads to almost identical curves. The effect of the zero-field mobility and the field dependency prefactor γ on IV and ZV curves is shown in A.4.

Figure 5.7 compares the magnitudes of the three components of the injection current with the total device current. In figure 5.7A a calculation is shown for a hole-only device with $\phi_S = \phi_T$ = 0.1 eV. In figure 5.7B a calculation is shown for a hole-only device with ϕ_S = 0.6 eV, ϕ_T = 0.1 eV. Bulk parameters are the same as above. In both cases, the interface recombinaton current nearly cancels the sum of the tunneling current and thermionic emission components. The actual device current is much smaller than the individual injection current components. For the device with the high hole injection barrier at positive bias, tunneling becomes dominant at high positive voltages. For the device with the low barrier for injection thermionic emission is dominant. In this case the concept of a triangular tunneling barrier and associated tunneling distance in the polymer is not valid anymore. Therefore, the integration of the field was done starting at the injection contact.

Figure 5.9 shows a calculated ZV curve for a hole-only device with tip-sample current I_t = 0.05 nA and a effective tip surface area A = 100 Å^2. Barrier height for injection at positive bias is 1.4 eV, at negative bias 1.3 eV. Parameters used for the bulk conduction are N_{DOS} = 1e27 m^{-3}, γ = 5.4e-4 $(m/V)^{1/2}$, $\mu(0)$ = 5e-11 m^2/Vs, T = 295 K, $\varepsilon = 3\varepsilon_0$. The black curve is calculated using m^* =

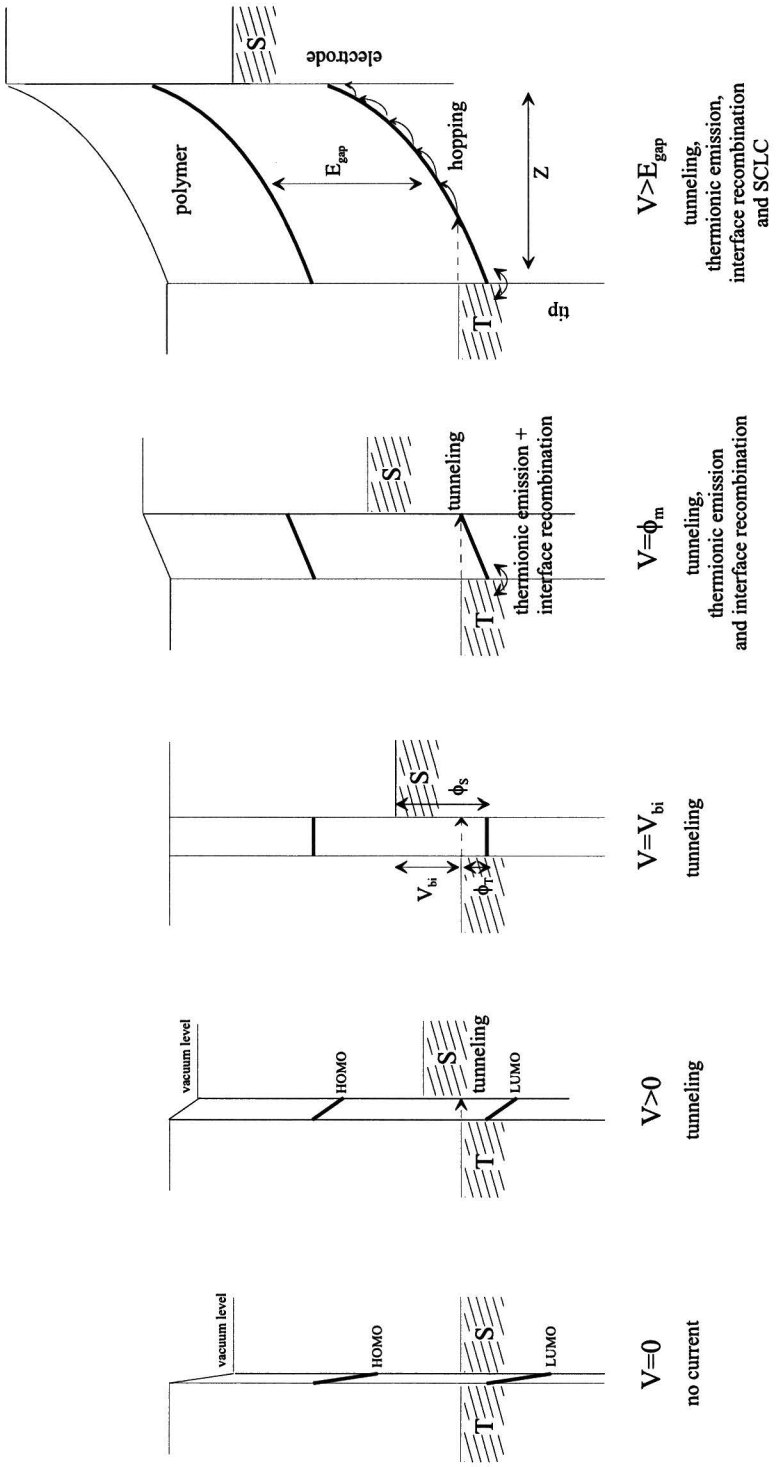

Figure 5.4: Proposed band diagram for hole-dominated device with unequal barrier heights to injection. Note the increasing thickness with increasing voltage, which is needed to keep I_t constant. T indicates the tip, S indicates the sample electrode.

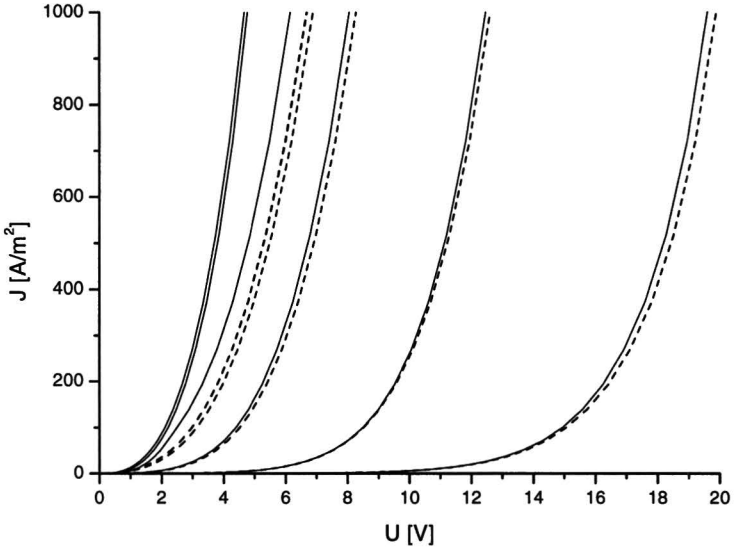

(A)

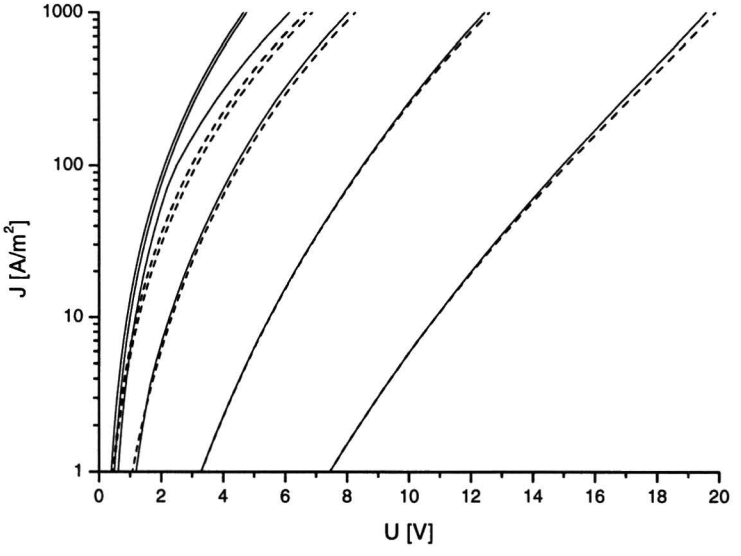

(B)

Figure 5.5: Calculated IV curves with barrier heights of ϕ_b = 0.1, 0.2, 0.3, 0.4, 0.5 and 0.6 eV (from left to right). Parameters used are N_{DOS} = 1e27 m^{-3}, γ = 3.2e-4 $(m/V)^{1/2}$, $\mu(0)$ = 1.7e-11 m^2/Vs, T = 295 K, $\varepsilon = 3\varepsilon_0$ and L = 120 nm. The dashed lines are calculated using the model proposed by [16]. The solid lines are calculated using the model proposed in this work. The dashed lines with ϕ_b = 0.2 and 0.3 eV are very close to each other. The difference between ϕ_b = 0.1 and 0.2 eV cannot be distinguished.

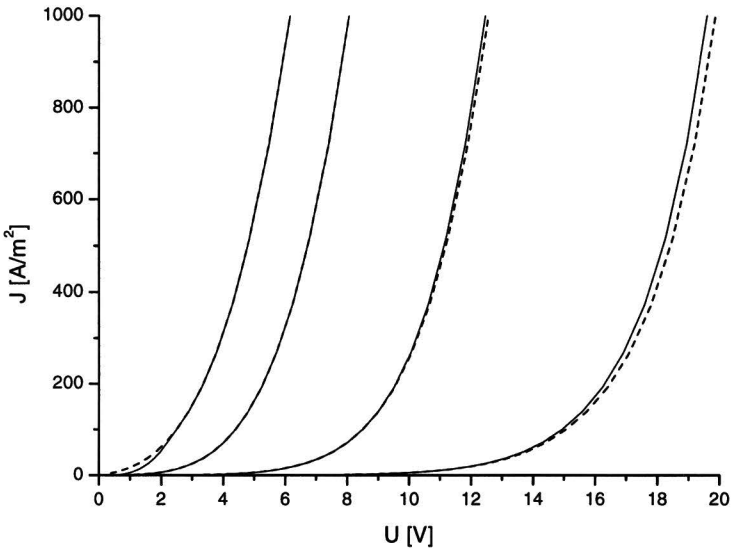

(A)

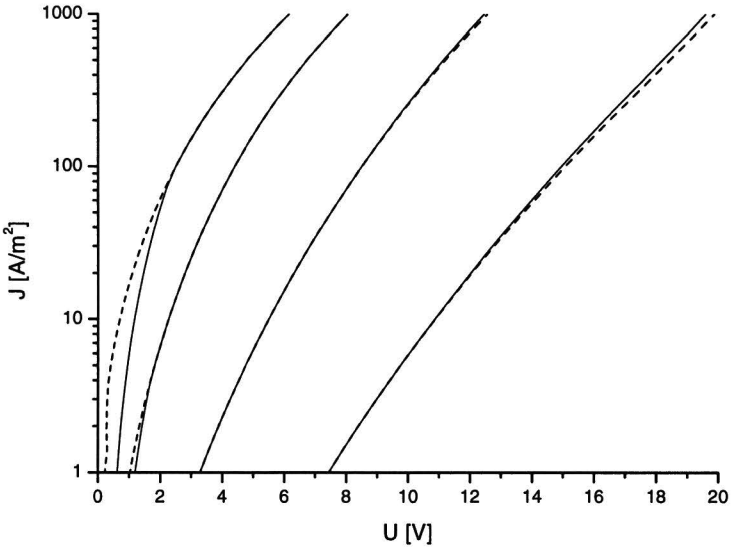

(B)

Figure 5.6: Calculated IV curves with barrier heights of ϕ_b = 0.3, 0.4, 0.5 and 0.6 eV (from left to right). Dashed lines are curves calculated with a Fowler-Nordheim expression for the tunneling current, solid lines are curves calculated with equation 5.5 for the tunneling current. Parameters used are N_{DOS} = 1e27 m^{-3}, γ = 3.2e-4 $(m/V)^{1/2}$, $\mu(0)$ = 1.7e-11 m^2/Vs, T = 295 K, $\varepsilon = 3\varepsilon_0$ and L = 120 nm.

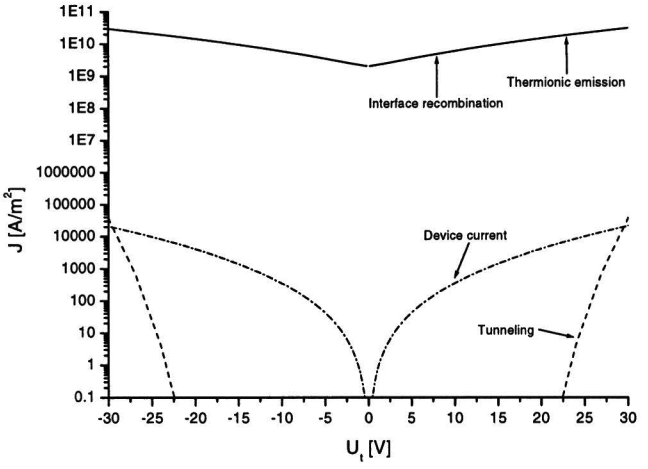

(A)

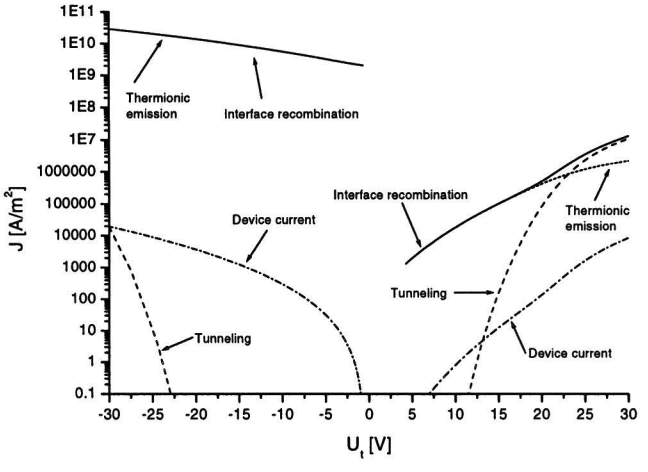

(B)

Figure 5.7: Calculated values of the injection current components and the total device current as a function of applied voltage for a hole-only device. A: Device with $\phi_S = \phi_T = 0.1$ eV. B: Device with $\phi_S = 0.6$ eV, $\phi_T = 0.1$ eV. Parameters used are $N_{DOS} = 1e27$ m^{-3}, $\gamma = 3.2e\text{-}4$ (m/V)$^{1/2}$, $\mu(0) = 1.7e\text{-}11$ m^2/Vs, $T = 295$ K, $\varepsilon = 3\varepsilon_0$ and $L = 120$ nm. For device A, integration of the field was done starting at the injection contact. In this case, omission of the tunneling current component does not influence the device current, since it is much lower than both the interface recombination or thermionic emission. For the device B tunneling becomes dominant at high voltages. At negative bias the current components for both devices are as shown in (A), but shifted over 0.5 V for device B.

m_e. The grey curve is calculated using $m^*= 4\ m_e$. This figure can be compared with the measurement done by [30] for a poly(1,12)AOPV-*co*-PPV thin film deposited on Au(111), which is shown in figure 5.8. The relative tip-height zero axis as used by [30] is indicated with the horizontol dashed line in figure 5.9. The vertical dashes lines indicate the onset of space charge limited conduction, which occurs when the tip-sample voltage is large enough for injection into the polaron levels.

The flat region in the curve is the result of direct tunneling through the polymer layer as is described in the previous section. We find that the slope and height of the flat region in figure 5.9 is determined by the barrier height, the current density, which depends on the choice of the effective tip surface, and the effective mass of the carriers. The effective mass of the carriers is determined by the width of the almost cosinusoidal dispersion relation over the first Brillouin zone. For transport perpendicular to the molecular axis, this is in the range of 0.2 to 0.5 eV for PPV which leads to $m^* = 5$ to 2 m_e [2].

The width of the flat region in figure 5.8 is interpreted by [30] as the energy gap between the hole-polaron (π^+) and electron-polaron level (π^-). If the voltage applied to the tip is +1.3 V then injection of holes into the π^+ level would be possible. If the voltage applied to the tip is -1.35 V then injection of electrons in the π^- level would be possible.

This, however, is not correct according to our model. In figure 5.10 we show a simplified band diagram for positive and negative bias, corresponding to figure 5.9. In this case, if the voltage applied to the sample equals -ϕ_S , the tip acts as a hole injector. If the voltage applied to the sample equals ϕ_T , the sample electrode acts as a hole injector. Therefore, the width of the flat region in the figure is simply the sum of the injection barriers into the π^+ level, which is $\phi_S + \phi_T$. In fact, the apparent gap observed in our measurements (chapter 6) is found to be equal to $\phi_S + \phi_T$.

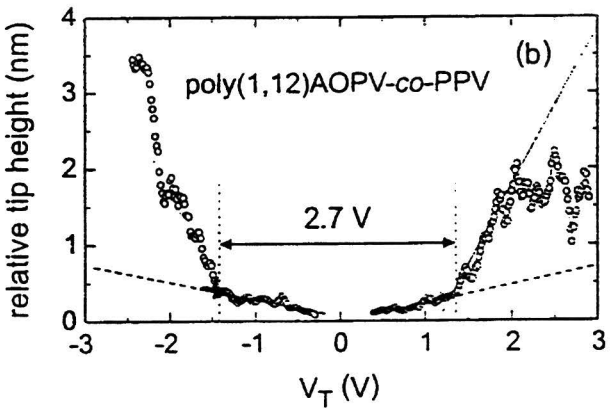

Figure 5.8: Typical relative tip height vs. tip voltage for poly(1,12)AOPV-*co*-PPV (I_t = 50 pA) thin film depositied on Au(111). Measurement done by [30].

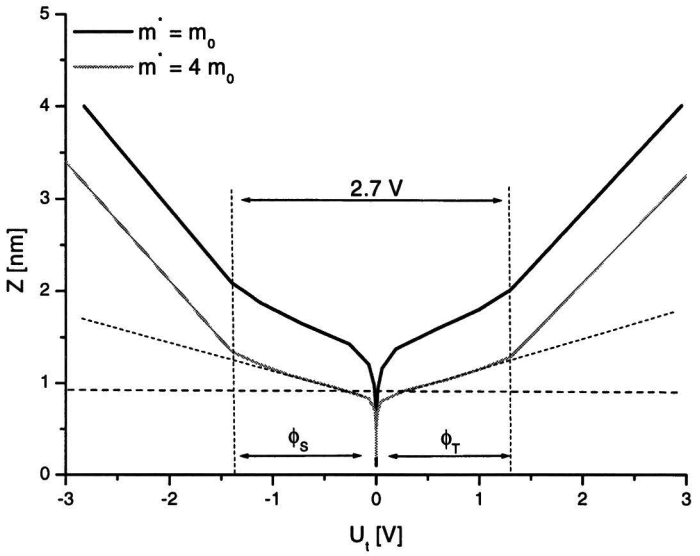

Figure 5.9: Calculated ZV curve for a tip-sample current $I_t = 0.05$ nA and a effective tip surface area $A = 100$ ^{2}. Barrier height to injection for positive bias is 1.4 eV, for negative bias 1.3 eV. Parameters used for the bulk conduction are N_{DOS} = 1e27 m^{-3}, γ = 5.4e-4 (m/V)$^{1/2}$, $\mu(0)$ = 5e-11 m^2/Vs, T = 295 K, $\varepsilon = 3\varepsilon_0$. The black curve is calculated using $m^* = m_e$. The grey curve is calculated using $m^* = 4\ m_e$. The horizontal dashed line indicates the relative tip-height zero axis for the grey curve as used figure 5.8. The vertical dashed lines denote the onset of injection into the polaron bands.

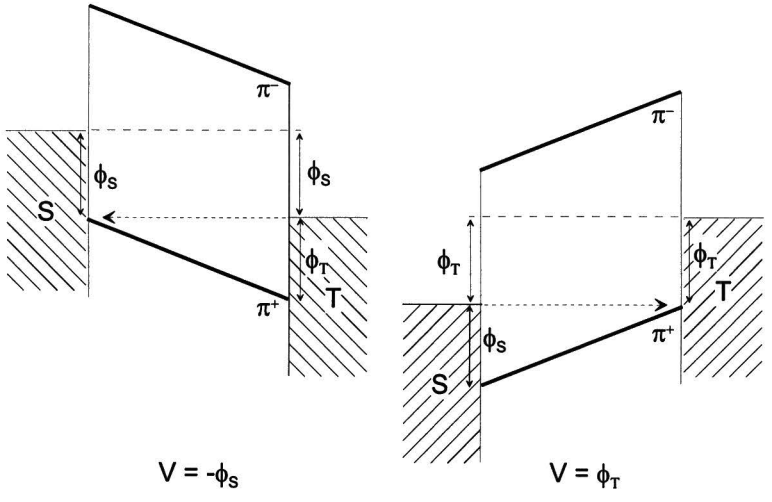

Figure 5.10: Simplified band scheme for the onset of injection into the hole-polaron level at positive and negative bias.

Chapter 6

Measurements

6.1 Introduction

In this chapter the measurements are presented. The chapter is organised in the following order: in section 6.2 the measurements on PPV/Au are discussed, in section 6.3 the measurements on PPV/Yb are discussed and in section 6.4 the measurements in P3HT/Au are discussed.

6.2 PPV/Au measurements

6.2.1 IV measurements

In figure 6.1 the IV measurements on PPV/Au samples are presented. IV curves were taken using a setpoint voltage of $U_t = 10$ V and setpoint currents $I_t = 0.02$, 0.1, 0.5, 1.0, 3.0 and 5.0 nA. Solid lines are line fits using a zero field mobility $\mu_p(0) =$ 5e-11 m^2/Vs, with a field dependency prefactor $\gamma =$ 5.4e-4 $(m/V)^{1/2}$. These parameters are identical to those used by [26] for MDMO-PPV samples. For the HOMO density of state $N_{DOS} =$ 1e27 m^{-3} is used [12]. The tip-sample electrode distance D_{set}, and barrier heights ϕ_S and ϕ_T are treated as fitting variables. As is expected from the model, the tip-sample electrode distance D_{set} varies with current from 70 nm at $I_t = 0.02$ nA to 38 nm at $I_t = 5$ nA. The workfunction of the Platinum tip is expected to be approximately 5.6 eV. The workfunction of the Gold sample electrode is known to be variable over a range of 4.5 to 5.4 eV. MDMO-PPV is expected to have an ionization potential of 5.1 to 5.2 eV, and an estimated electron affinity of 2.6 to 3.1 eV [5]. From these values we expect the Platinum tip to be an Ohmic contact, and the Gold electrode to have a hole injection barrier of 0.7 to -0.3 eV. However, the barrier height we found from our experiments for injection into the hole polaron level could be taken equal for both contacts, and varied with current between 0.45 to 0.52 eV. This is within the range expected for the Gold electrode. The injection barriers found for the Platinum tip can be explained by (oxygen) contamination of the tip and the mechanical nature of the tip/polymer contact.

The IV curves shown in figure 6.1 are averaged IV curves. Only curves which go through the setpoint were taken in the averaging. Figure 6.2 shows a set of unaveraged IV curves for $U_t = 10$ V, $I_t = 1.0$ nA. As can be seen in the

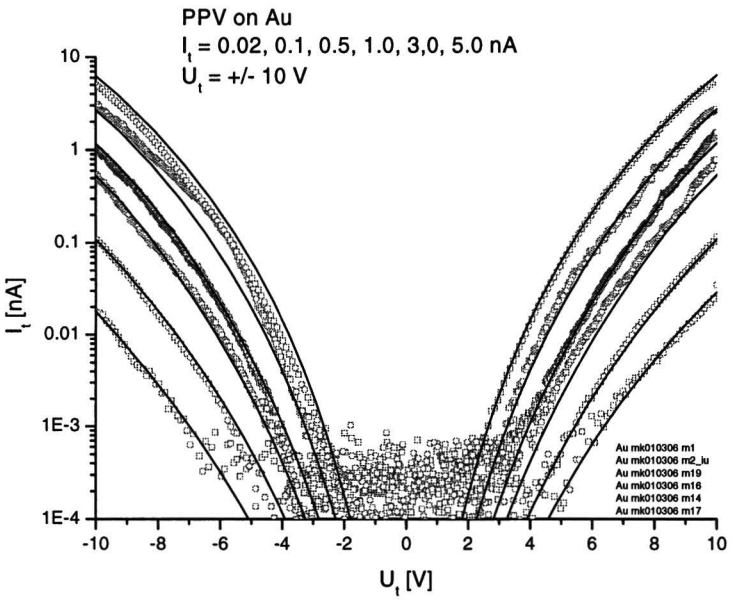

Figure 6.1: IV curves measured on PPV/Au samples. Setpoints are U_t = +/-10 V, I_t = 0.02, 0.1, 0.5, 1.0, 3.0 and 5.0 nA. Solid lines are line fits using $\mu_p(0)$ = 5e-11 m^2/Vs, γ = 5.4e-4 $(m/V)^{1/2}$, N_{DOS} = 1e27 m^{-3}. D_{set} and ϕ_S = ϕ_T range from 70 to 38 nm and 0.52 to 0.45 eV resp., for I_t = 0.02 to 5.0 nA.

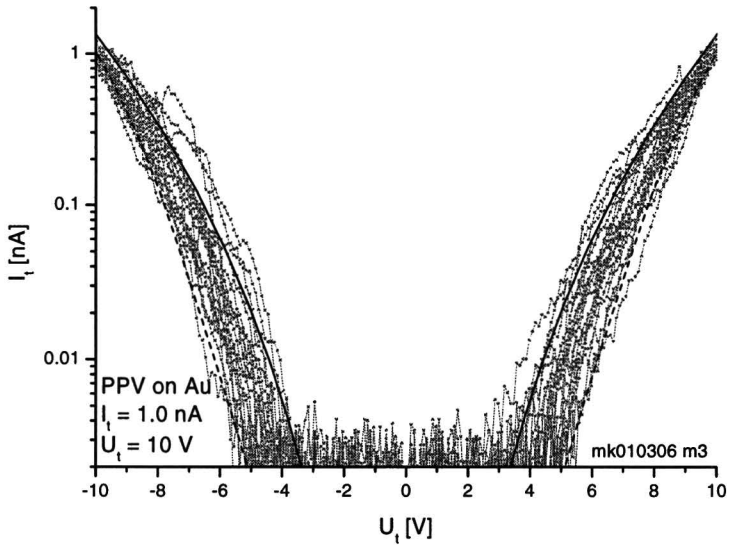

Figure 6.2: Spread in IV curves measured on PPV/Au samples, U_t = 10 V, I_t = 1.0 nA. Solid and dashed lines are line fits using $\mu_p(0)$ = 5e-11 m^2 /Vs, γ = 5.4e-4 $(m/V)^{1/2}$, N_{DOS} = 1e27 m^{-3} . For the solid lines D_{set} = 45 nm, ϕ_S = ϕ_T = 0.53 eV, for the dashed lines D_{set} = 47 nm, ϕ_S = ϕ_T = 0.43 eV.

figure there is a lot of spread in individual IV curves. This can be attributed to variations in barrier height to injection. The solid lines are calculated using hole injection barriers of 0.53 eV for both contacts, whereas the dashed lines are calculated using hole injection barriers of 0.43 eV. The variation in barrier height of 0.1 eV can be attributed to the inhomogeneous nature of the polymer/metal interface.

6.2.2 ZV measurements

Figure 6.3 shows a set of unaveraged ZV curves, measured using a setpoint of U_t = 10 V, I_t = 1 nA. The variation in tip-sample electrode distance at the setpoint agrees well with the tip-sample electrode distance fitting parameter D_{set} used for the IV curves above. The solid line is a calculated ZV curve using barriers heights for hole injection of 0.5 eV, which compares favourably to the IV curves. The zero-field mobility used for the calculation is $\mu_p(0)$ = 1e-11 m^2/Vs. There are two problems with this result: firstly, the choice of equal barrier heights does not reproduce the asymmetry between the two polarities observed in the measurement, and secondly, the model does not reproduce the wiggles in the curve.

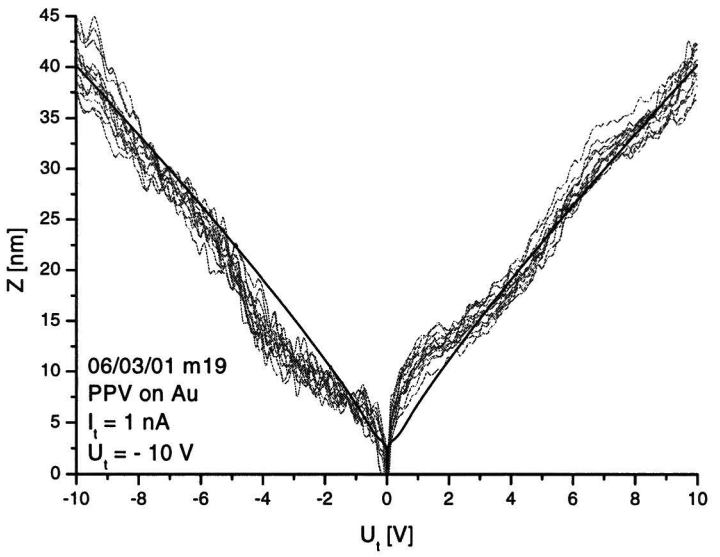

Figure 6.3: Typical ZV measurement on PPV/Au sample, U_t = -10 V, I_t = 1 nA. Solid lines are fits using $\mu_p(0)$ = 1e-11 m^2 /Vs, γ = 5.4e-4 $(m/V)^{1/2}$, N_{DOS} = 1e27 m^{-3} , $\phi_S = \phi_T$ = 0.5 eV.

To reproduce the asymmetry as observed in the measurement, the curves were fitted with a hole injection barrier height for positive bias of ϕ_S = 0.1 eV and a hole injection barrier height for negative bias of ϕ_T = 0.15 eV, which is shown in figure 6.4. For clarity, only the voltage range between -1 V and +1 V is shown, together with a plot of the average tip-sample current during the ZV

measurements. As can be seen, the strong decrease of tip-sample distance in the voltage range between -0.2 and 0.2 V is not an artefact and can be modelled by low injection barriers. We conclude that direct tunneling through through a barrier given by the position of the hole polaron level relative to the Fermi level is the explanation for the observed behavior.

A possible explanation for the observed wiggles in the measured ZV curves is the buildup of negative induced charges near the positive contact and positive charges near the negative contact, causing bandbending near the interface as is shown in figure 6.5. Mobile charges may be present in our sample because of doping caused by exposure to air and residues of the solvent used for spincoating. To reproduce the effect of bandbending, an exponential distribution of charge near both contacts was superimposed onto the charge distribution as described by the model:

$$\frac{dE}{dx} = \frac{J_D}{\varepsilon\mu(0)\exp(\gamma\sqrt{E})\,E} + \frac{e}{\varepsilon}N(x)$$

where

$$N(x) = N_+ \exp\left(-\left(\frac{x-Z}{X_\sigma}\right)^2\right) - N_- \exp\left(-\left(\frac{x}{X_\sigma}\right)^2\right) \qquad (6.1)$$

with $N_+ = N_- =$ 5e25 m^{-3} , $X_\sigma =$ 5 nm and Z the separation between both contacts. Note that in the calculation the negative charge distribution is placed at the onset of space charge limited conduction and not at the injecting contact. For a charge distribution placed at the injecting contact, bandbending and tunneling should be calculated self-consistently. If we assume that injection is Ohmic, i.e. the tunneling distance into the polymer is zero, which is inconsistent with figure 6.4, the calculation is correct.

The result is shown in figure 6.6. The other parameters used are $\mu_p(0) =$ 1e-10 m^2/Vs, $\gamma =$ 5.4e-4 $(m/V)^{1/2}$, $N_{DOS} =$ 1e27 m^{-3} , $\phi_S =$ 0.1 eV, $\phi_T =$ 0.15 eV. As can be seen in the figure the wiggles in the curve are described by 6.1. The same procedure is followed for the ZV curves shown in figure 6.7. Both measurements are performed using a setpoint of $U_t =$ 10 V, $I_t =$ 1 nA. The large differences in Z range can be attributed to local variations of γ. These variations take place over a scale of 5 nm in lateral direction. Tabel A.1 shows the specific parameters used in the fits of the separate branches.

6.2.3 IZ measurements

Figure 6.8 shows a typical IZ measurement using a setpoint of $U_t =$ -10 V, $I_t =$ 0.02 nA. The IZ curve was taken by first retracting the tip over a distance of 10 nm, and subsequently moving the tip down over a range of 20 nm while measuring the current. Currents below approximately 5 pA fall within the noise level of the current amplifier. The solid line is a calculated IZ curve using parameters $\mu_p(0) =$ 5e-11 m^2/Vs, $\gamma =$ 5.4e-4 $(m/V)^{1/2}$, $N_{DOS} =$ 1e27 m^{-3} , $\phi_S = \phi_T =$ 0.65 eV, $D_{set} =$ 50 nm. Compared to values found for IV curves, we would expect a barrier height of 0.5 ± 0.05 eV, and $D_{set} =$ 70 nm. A lower barrier height leads to a higher D_{set} but also decreases the slope of the curve, which is not observed in the measurements. Changing the other parameters does

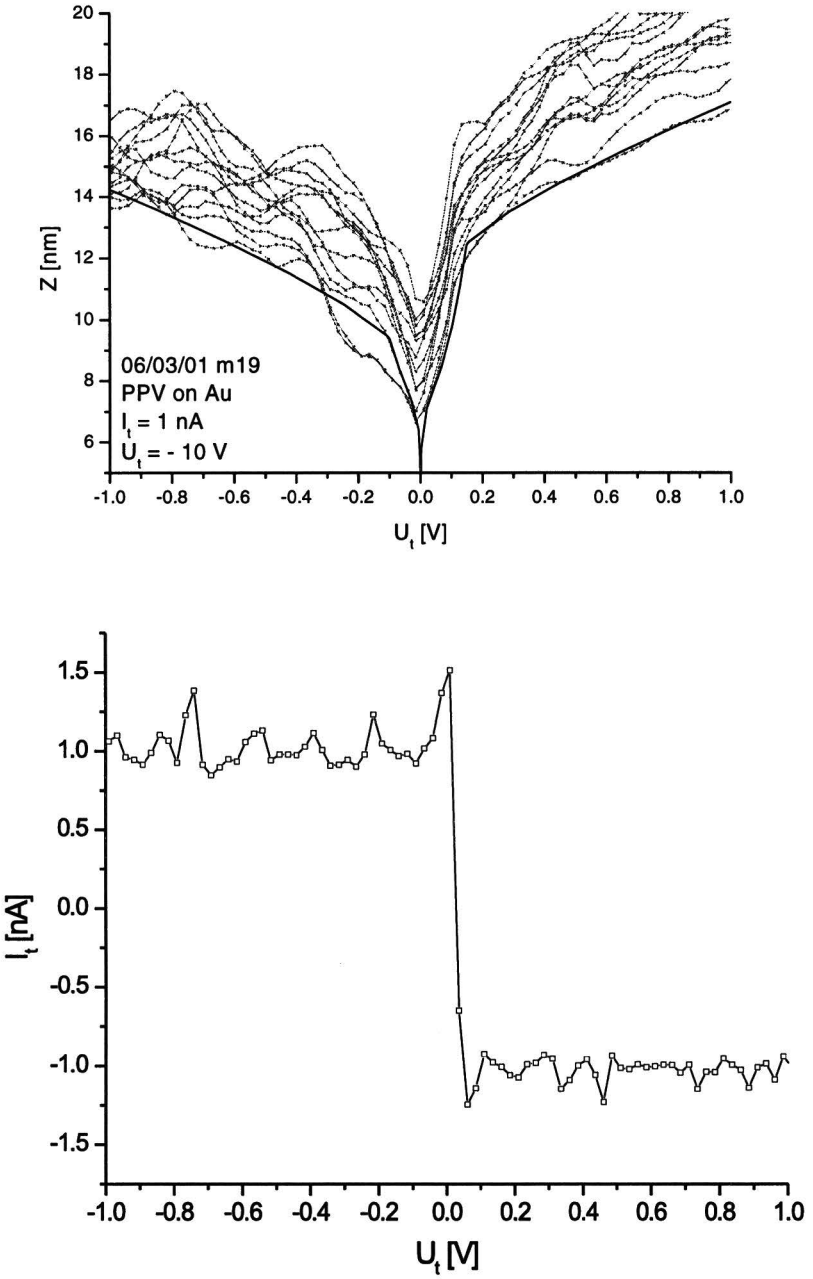

Figure 6.4: Top: low voltage part of ZV measurement on PPV/Au sample, U_t = -10 V, I_t = 1 nA. The solid line is a calculated curve using $\mu_p(0)$ = 1e-11 m^2 /Vs, γ = 5.4e-4 $(m/V)^{1/2}$, N_{DOS} = 1e27 m^{-3} , ϕ_S = 0.1 eV, ϕ_T = 0.15 eV. Bottom: IV curve during ZV measurement showing that the current is constant.

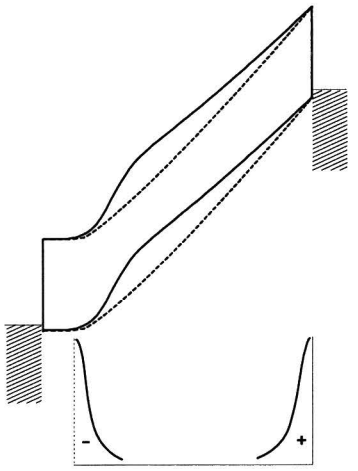

Figure 6.5: Solid lines indicate bandbending of the polymer bands caused by induced charges near the contacts. The dashed lines indicate the shape of the bands as described by the model without the exponential charge distributions.

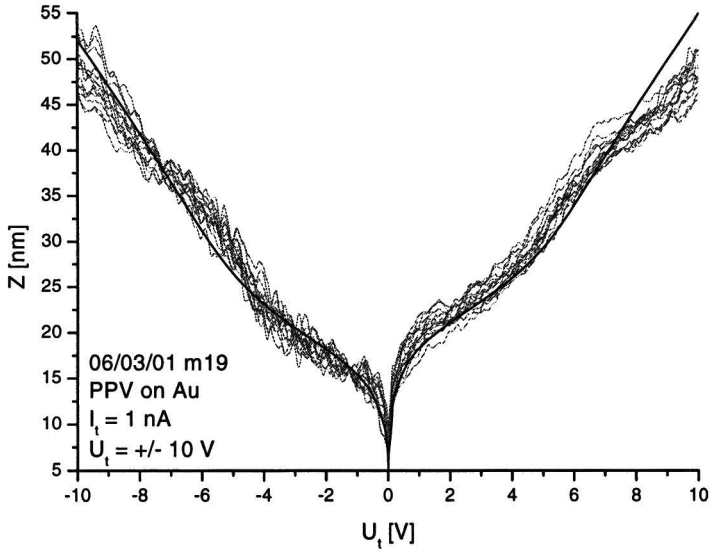

Figure 6.6: ZV measurement on PPV/Au sample, U_t = -10 V, I_t = 1 nA. $\mu_p(0)$ = 1e-10 m^2/Vs, γ = 5.4e-4 $(m/V)^{1/2}$, N_{DOS} = 1e27 m^{-3} , ϕ_S = 0.1 eV, ϕ_T = 0.15 eV. The wiggles in the curve are fitted using a superposition of exponential charge distributions near the contacts.

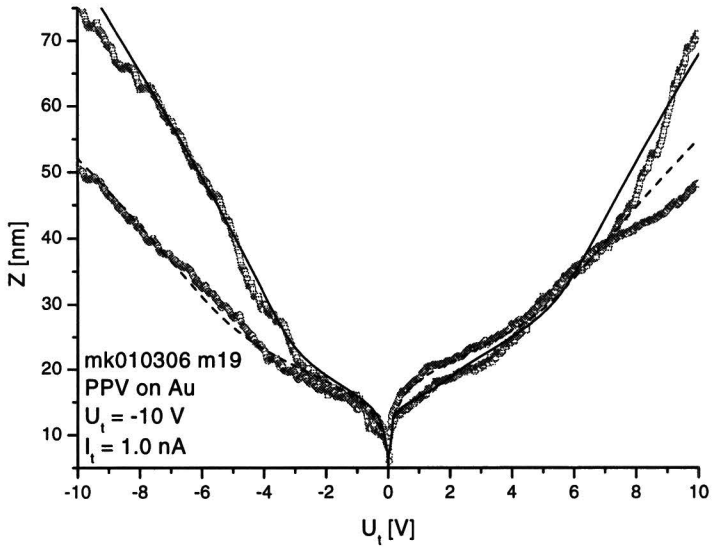

Figure 6.7: ZV measurements on PPV/Au sample, with setpoint U_t = -10 V, I_t = 1 nA. N_{DOS} = 1e27 m^{-3}, solid lines: ϕ_S = 0.15 eV, ϕ_T = 0.15 eV $\mu_p(0)$ = 1e-10 m^2 /Vs, γ = 8e-4 $(m/V)^{1/2}$, dashed lines: ϕ_S = 0.1 eV, ϕ_T = 0.15 eV $\mu_p(0)$ = 1e-10 m^2 /Vs, γ = 5.4e-4 $(m/V)^{1/2}$, ϕ_S = 0.1 eV, ϕ_T = 0.15 eV.

not yield satisfying results. We conclude that although the parameters for the calculated IZ curves are not in perfect agreement with those of the IV curves, it is clear that the conduction can be described by the model and not by tunneling through a vacuum barrier to the surface of the polymer layer, which would result in a much stronger dependence of current with tip-sample distance. The lack of topography in our measurements is explained by the absence of tunneling to the surface of the polymer film through a vacuum barrier.

6.3 PPV/Yb measurements

6.3.1 IV measurements

Figure 6.10 shows the measured IV curves for PPV samples with an Yb electrode. IV curves were measured using a setpoint of U_t = -10 V, I_t = 0.02, 0.1, 0.5, 1.0, 2.0 and 5.0 nA. The IV curves with $I_t > 0.5$ nA are symmetrical, whereas IV curves with $I_t < 0.5$ nA are asymmetrical around $U_t = 0$ V. In the upper part of figure 6.11 a set of IV curves is shown with the setpoint current between $I_t = 0.1$ and 0.5 nA, in the lower part a set of IV curves with $I_t = 0.5$ nA are shown on a linear scale. The observed asymmetry is expected because of the workfunction difference of the Yb electrode and the Platinum tip. Ytterbium is expected to have a workfunction of approximately 2.8 eV. The workfunction of the Platinum tip is expected to be approximately 5.6 eV. Figure 6.9 shows

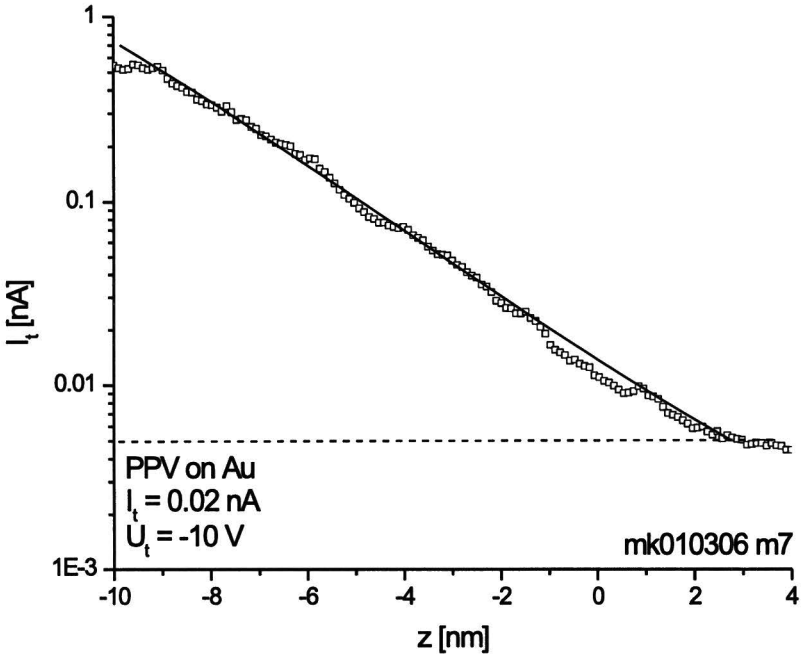

Figure 6.8: IZ curve, PPV on Au, U_t = -10 V, I_t = 0.02 nA, $\mu_p(0)$ =5e-11 m^2 /Vs, γ = 5.4e-4 $(m/V)^{1/2}$, N_{DOS} = 1e27 m^{-3} , $\phi_S = \phi_T$ = 0.65 eV, D_{set} = 50 nm. The dashed line indicates the noise level of current amplifier.

the simplified bandscheme for positive and negative bias. When the sample is biased positively, injection into either polaron level is very difficult because of the high injection barriers, and conduction is low. When the sample is biased negatively, injection is expected to be close to Ohmic.

The solid lines in figure 6.10 are calculated curves using identical values as for the PPV/Au measurements: $\mu_p(0)$ = 5e-11 m^2/Vs, γ = 5.4e-4 $(m/V)^{1/2}$, N_{DOS} = 1e27 m^{-3}. Calculated tip-sample electrode distances are D_{set} = 38 to 70 nm and barriers to hole injection from sample resp. tip are $\phi_S = \phi_T$ = 0.43 to 0.53 eV. The negative branch of all measured IV curves is well described using these parameters. However, barriers for hole injection from the sample are taken equal to the barriers for hole injection from the tip, which is not in accordance with our expectations, as outlined above. Therefore, the measurements in figure 6.11 have been fitted with unequal barriers to hole injection, using D_{set} = 51 nm, ϕ_T = 0.49 eV, ϕ_S = 0.59 eV for the dashed lines, and D_{set} = 56 nm, ϕ_T = 0.53 eV, ϕ_S = 0.61 eV for the solid lines. These values for hole injection from the sample are much smaller than the expected value of about 2.8 eV, and it is obvious that the model does not describe accurately the observed currents for positive sample bias. The fact that relatively large currents are observed in our measurements for positive sample bias, leads to the conclusion that either the positive bias current is not due to carriers which are injected into the polaron level, but more likely due to the transport through impurity levels in the material, or that

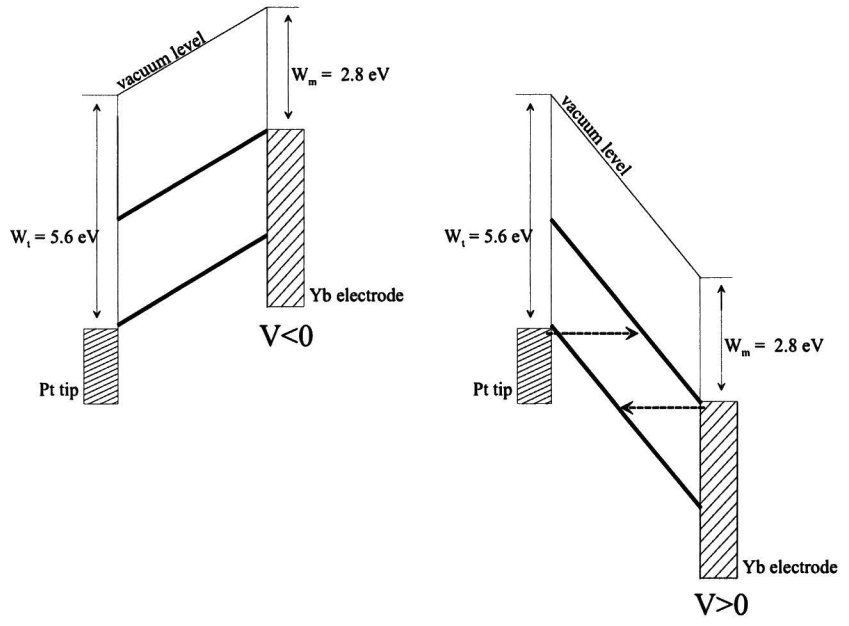

Figure 6.9: Simplified picture showing high barriers to injection for positive sample bias, Ohmic contacts for negative sample bias.

the injection barriers are effectively lowered by large bandbending effects near the injecting interface. Transport through impurity levels has been described qualitatively by Poole-Frenkel emission [16] which has the form [32]

$$J_{PF} \sim E \exp\left[-\frac{q(\phi_{PF} - \sqrt{qE/\pi\varepsilon})}{k_B T}\right]$$

for transport through a single discrete impurity level. The $\sqrt{E}$ dependence on $\log(J)$, however, has not been observed in our measurements.

6.3.2 ZV measurements

In figure 6.12 a ZV measurement is shown for I_t = 0.02 nA and U_t = -10 V. The negative and positive branch for the Yb samples were obtained seperately since the voltage was not ramped through zero. Therefore the Z values shown are relative and indicate a minimum tip-sample electrode distance. The negative branch shows a kink at -3 V which is expected from the theoretical alignment of the π^+ level and the Yb Fermi level and can be explained as the threshold voltage for transport through the π^+ level. The solid line in the figure is the calculated ZV curve using the parameters $\mu_p(0)$ = 5e-11 m^2/Vs, γ = 1e-4 $(m/V)^{1/2}$, N_{DOS} = 1e27 m^{-3} and barriers for hole injection from tip and sample of ϕ_T = 0.55 eV resp. ϕ_S = 2.8 eV. In figure 6.13 a corresponding IV measurement is shown which has been fitted with the same parameters except for γ, which was taken to be 5.4e-4 $(m/V)^{1/2}$. For both figures, the negative branch is fairly good described by the calculated curves, the positive branch, however, requires a much lower injection barrier and falls outside the scale of figure 6.13. Although the kink in

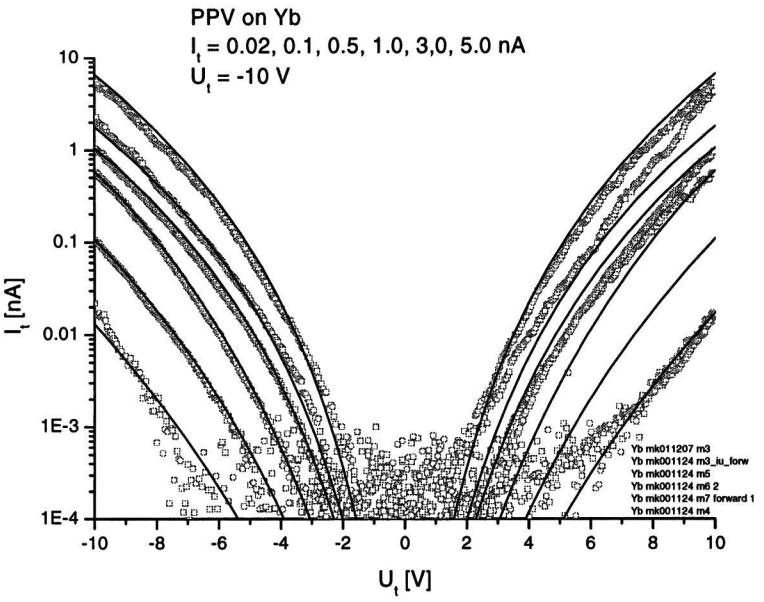

Figure 6.10: IV curves taken on PPV/Yb samples. Setpoints are U_t = - 10 V, I_t = 0.02, 0.1, 0.5, 1.0, 2.0 and 5.0 nA. Solid lines are line fits using $\mu_p(0)$ = 5e-11 m^2/Vs, γ = 5.4e-4 $(m/V)^{1/2}$, N_{DOS} = 1e27 m^{-3}, D_{set} = 38 to 70 nm, $\phi_S = \phi_T$ = 0.43 to 0.53 eV.

the negative branch of the ZV measurement has unambigiously been observed in some of the measurements, it is not observed in all measurements. Figure 6.14 shows a ZV measurement for U_t = 10 V, I_t = 0.1 nA, which doesn't show any kinks and could be fitted with $\mu_p(0)$ = 5e-11 m^2/Vs, γ = 5.4e-4 $(m/V)^{1/2}$, N_{DOS} = 1e27 m^{-3} and $\phi_S = \phi_T$ = 0.5 eV. We conclude that the relaively small barriers found for hole injection in the positive bias might be explained by transport through impurity states, or lowering of the barrier by bandbending, caused by the presence of oxygen or residues of the solvent used for spincoating. The kinks observed in some ZV measurements are most likely due to either small regions where the band alignment is as theoretically expected, or due to extreme bandbending near the Yb electrode. The latter is similar to what is discussed in section 6.2.2.

6.4 P3HT measurements

P3HT measurements were performed to investigate the effect of a higher carrier mobility. Two typical IV measurements done on P3HT with a Gold electrode are shown in figure 6.15. A measurement with U_t = 10 V, I_t = 0.5 nA is indictated by the open circles. A measurement with U_t = 10 V, I_t = 0.1 nA is indictated by the open squares. P3HT is known for its large variety in mobility and the samples were expected to be inhomogeneous. Therefore, all parameters were treated as fitting parameters. The open circles could be fitted with $\mu_p(0)$ = 1e-9 m^2/Vs, γ = 3e-4 $(m/V)^{1/2}$, N_{DOS} = 1e28 m^{-3}, D_{set} = 45 nm, ϕ_S =

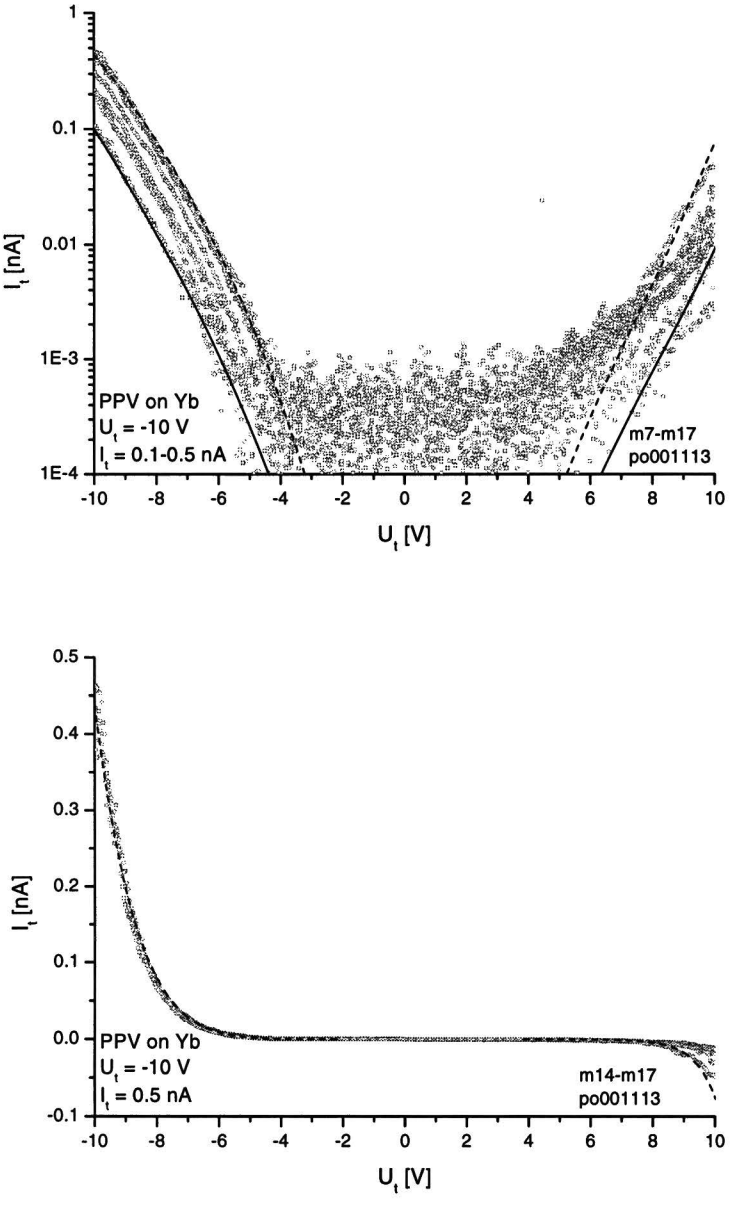

Figure 6.11: IV curves taken on PPV/Yb samples. Setpoints are U_t = - 10 V, I_t = 0.1, 0.2, 0.3, 0.4, and 0.5 nA. The lower figure shows the IV curve for I_t = 0.5 nA on a linear scale. The dashed lines are fits using $\mu_p(0)$ = 5e-11 m^2/Vs, γ = 5.4e-4 $(m/V)^{1/2}$, N_{DOS} = 1e27 m^{-3}, D_{set} = 51 nm, ϕ_T =0.49 eV, ϕ_S = 0.59 eV. The solid lines are fits using $\mu_p(0)$ = 5e-11 m^2/Vs, γ = 5.4e-4 $(m/V)^{1/2}$, N_{DOS} = 1e27 m^{-3}, D_{set} = 56 nm, ϕ_T =0.53 eV, ϕ_S = 0.61 eV.

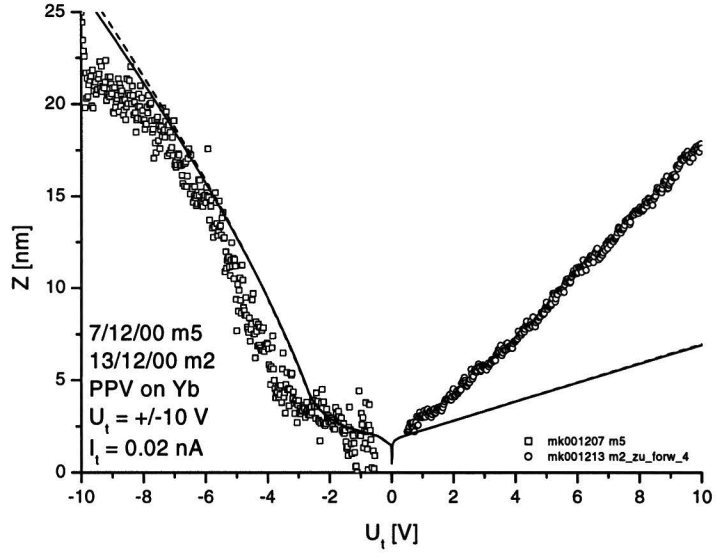

Figure 6.12: ZV curve PPV on Yb, U_t = +/-10 V, I_t = 0.02 nA. solid line: $\mu_p(0)$ = 5e-11 m^2 /Vs, γ = 1e-4 $(m/V)^{1/2}$, N_{DOS} = 1e27 m^{-3} , ϕ_T = 0.55 eV, ϕ_S = 2.8 eV, dashed line: $\mu_p(0)$ = 3e-11 m^2 /Vs, γ = 1e-4 $(m/V)^{1/2}$, N_{DOS} = 2e27 m^{-3} , ϕ_T = 0.56 eV, ϕ_S = 2.8 eV.

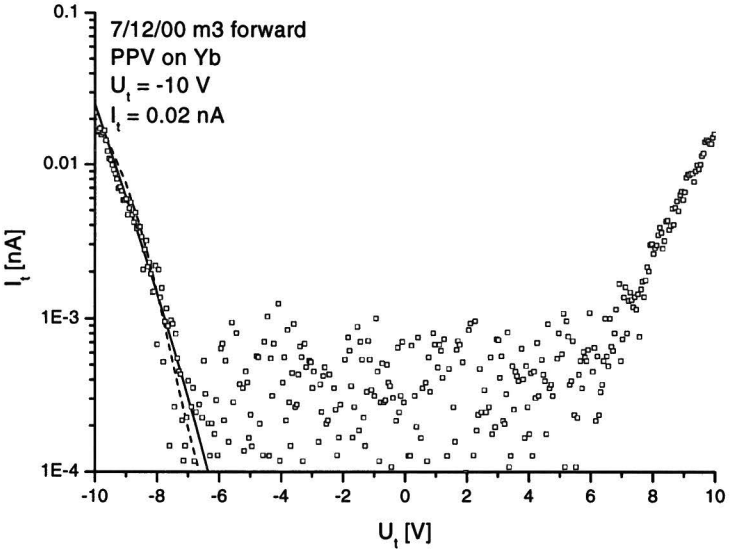

Figure 6.13: IV curve PPV on Yb, U_t = -10 V, I_t = 0.02 nA. solid line: $\mu_p(0)$ = 5e-11 m^2 /Vs, γ = 5.4e-4 $(m/V)^{1/2}$, N_{DOS} = 1e27 m^{-3} , ϕ_T = 0.55 eV, ϕ_S = 2.8 eV, D_{set} = 48 nm. dashed line: $\mu_p(0)$ = 3e-11 m^2 /Vs, γ = 2e-4 $(m/V)^{1/2}$, N_{DOS} = 2e27 m^{-3} , ϕ_T = 0.56 eV, ϕ_S = 2.8 eV, D_{set} = 31 nm.

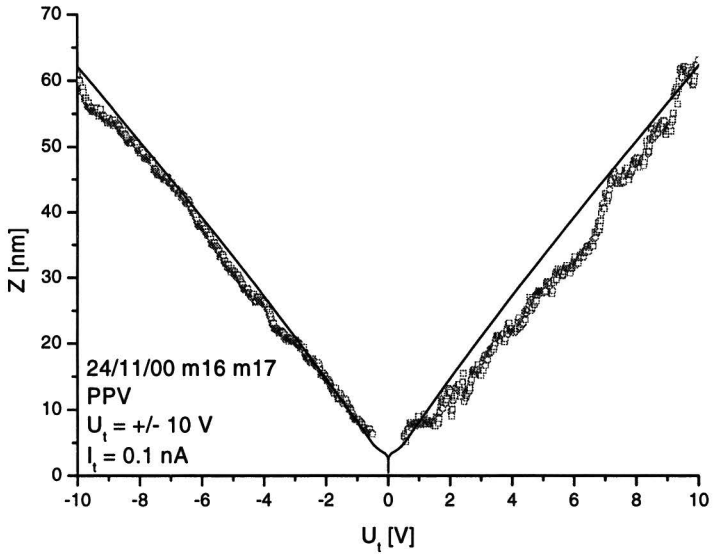

Figure 6.14: ZV curve PPV on Yb, U_t = +/-10 V, I_t = 0.1 nA. $\mu_p(0)$ = 5e-11 m^2 /Vs, γ = 5.4e-4 $(m/V)^{1/2}$, N_{DOS} = 1e27 m^{-3} , $\phi_S = \phi_T$ = 0.5 eV.

ϕ_T = 0.6 eV. The open squares could be fitted with $\mu_p(0)$ = 1e-6 m^2 /Vs, γ = 6e-4 $(m/V)^{1/2}$, N_{DOS} = 1e28 m^{-3}, D_{set} = 105 nm, $\phi_S = \phi_T$ = 0.56 eV. The mayor difference in these parameters is the mobility which is 3 decades higher for the open squares. The larger density of states used for P3HT compared to PPV can be expected from the different chemical structure [1]. The ZV measurements done on P3HT/Au show a spread which also can be attributed to inhomogenities leading to mobility differences. The measurements shown in figure 6.16 are performed using a setpoint of U_t = 10 V, I_t = 0.5 nA. Note the small wiggle in the positive branch. The dashed lines are fits using $\mu_p(0)$ = 1.5e-11 m^2/Vs, the solid lines are fits using $\mu_p(0)$ = 3e-10 m^2/Vs. The other parameters are γ = 6e-4 $(m/V)^{1/2}$, N_{DOS} = 1e28 m^{-3} , ϕ_S = 0.15 eV, ϕ_T = 0.1 eV. Figure 6.17 shows an IZ measurement performed using U_t = 10 V, I_t = 0.2 nA. The solid line is a calculated curve using $\mu_p(0)$ = 1e-6 m^2/Vs, γ = 6e-4 $(m/V)^{1/2}$, N_{DOS} = 1e28 m^{-3}, D_{set} = 91 nm, $\phi_S = \phi_T$ = 0.56 eV. We conclude that all measurements on P3HT can be described by the model.

The relatively small values of ϕ_S and ϕ_T found for the ZV curves, as compared to those found from the IV curves, might be explained by the effect of the local orientation of the polymer chains. Two possible orderings are known for P3HT. One which has a strong interchain overlap of p_z orbitals in the direction perpendicular to the substrate, i.e. the tunneling direction. The other has a small interchain overlap in this direction [11]. For the former situation the dispersion is large, and the tunneling mass is low. The latter situation has a higher tunneling mass. In either case, the real tunneling mass may be smaller than m_e which was used in the calculations. This has the same effect on the carrier injection as a lowering of the tunneling barrier height. The SCLC transport is

basically independent of the carrier mass. Therefore, the effect of barrier height and effective mass may be interchangable in the calculation.

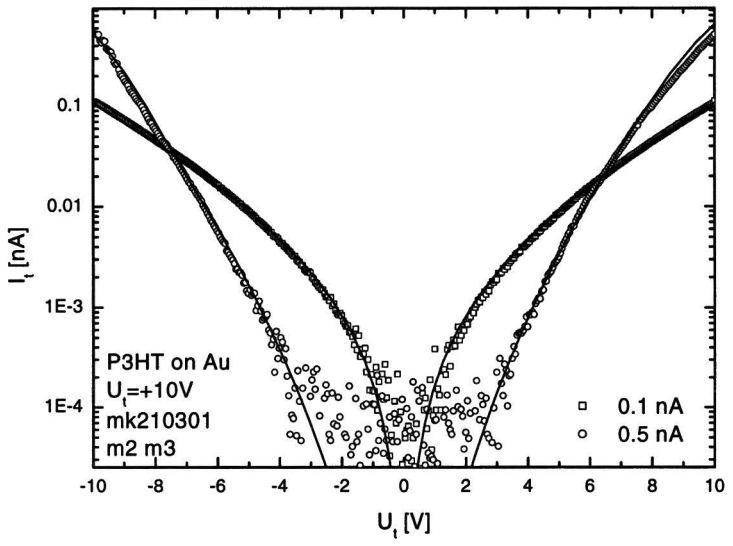

Figure 6.15: IV curve, P3HT on Au, U_t = 10 V, I_t = 0.1 nA and 0.5 nA. Fit done for 0.1: $\mu_p(0)$ = 1e-6 m^2 /Vs, γ = 6e-4 $(m/V)^{1/2}$, N_{DOS} = 1e28 m^{-3} ,D_{set} =105 nm, $\phi_S = \phi_T$ = 0.56 eV. Fit done for 0.5: $\mu_p(0)$ =1e-9 m^2 /Vs, γ = 3e-4 $(m/V)^{1/2}$, N_{DOS} = 1e28 m^{-3}, D_{set} = 45 nm, $\phi_S = \phi_T$ = 0.6 eV.

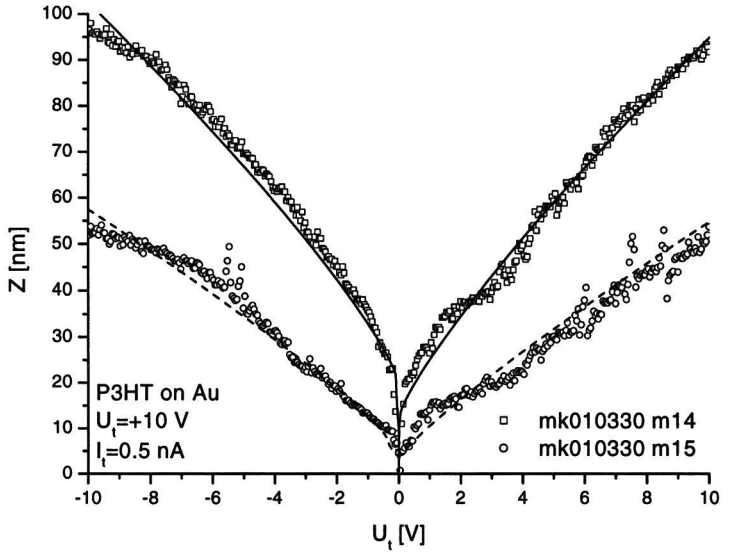

Figure 6.16: ZV curve, P3HT on AU, $U_t = 10$ V, $I_t = 0.5$ nA, dashed lines: $\mu_p(0) =$ 1.5e-11 m^2 /Vs, solid lines:$\mu_p(0) =$ 3e-10 m^2 /Vs. $\gamma =$ 6e-4 $(m/V)^{1/2}$, $N_{DOS} =$ 1e28 m^{-3} , $\phi_S = 0.15$ eV, $\phi_T = 0.1$ eV.

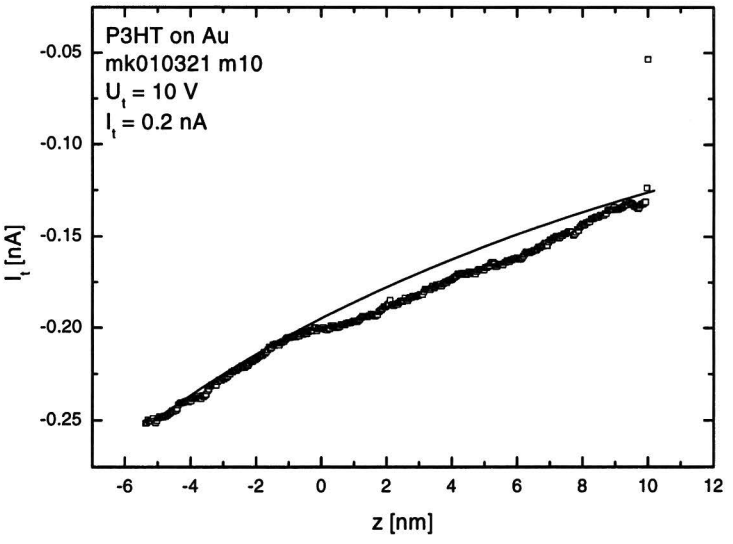

Figure 6.17: IZ curve. setpoint $U_t = 10$ V, $I_t = 0.2$ nA. Fit is done using $\mu_p(0)$ =1e-6 m^2 /Vs, $\gamma =$ 6e-4 $(m/V)^{1/2}$, $N_{DOS} =$ 1e28 m^{-3} , $D_{set} = 91$ nm, $\phi_S = \phi_T = 0.56$ eV.

Appendix A

Appendix

A.1 Complete elliptic integrals

The complete elliptic integrals of the first and second kind are given by

$$E(k) = \int_0^1 \frac{\sqrt{1-k^2t^2}}{\sqrt{1-t^2}}dt$$
$$K(k) = \int_0^1 \frac{1}{\sqrt{1-t^2}\sqrt{1-k^2t^2}}dt$$

A.2 Detailed balancing

The determination of the interface recombination prefactor $\nu = AT^2/N_{DOS}$ follows from detailed balancing of the currents flowing from the metal contact into the polymer (j_{12}) and vice versa (j_{21}) at zero bias. The key assumption of detailed balancing is that the ratio of the propabilities for a particle to move from state 1 to 2 (w_{12}) and vice versa (w_{21}) is given by a Boltzmann factor, where u_1 and u_2 are the energies of state 1 and 2 respectively:

$$\frac{w_{12}}{w_{21}} = \exp(-\frac{u_2-u_1}{k_BT}) \tag{A.1}$$

The current j_{12} is given by Fermi's golden rule and equal to the thermionic emission current density:

$$j_{12} = D_1 f_1 w_{12} D_2(1-f_2) = AT^2 \exp(-\frac{u_2-u_1}{k_BT})$$

where D_1 and D_2 are the density of states of the metal and polymer respectively, and f the Fermi-Dirac distribution. The metal can be considered as a infinite reservoir for uptake and emission, therefore we set $D_1 f_1 = D_m$. The density of states of the polymer is N_{DOS} and the polymers states are assumed to be empty, thus $f_2 = 0$, which gives the following expression for w_{12}:

$$w_{12} = \frac{AT^2 \exp(-\frac{u_2-u_1}{k_BT})}{D_m N_{DOS}} \tag{A.2}$$

The current j_{21} is equal to the interface recombination $\nu p(0)$:

$$j_{21} = D_2 f_2 w_{21} D_1 (1 - f_1) = \nu p(0)$$

where $D_2 f_2$ is the carrier density at the polymer side of the interface ($p(0)$) and $D_1(1 - f_2)$ is the number of free states in the metal (D_m), which results in the following expression for w_{21}:

$$w_{21} = \frac{\nu}{D_m}. \tag{A.3}$$

By substituting equation A.2 and A.3 into equation A.1 we find for the interface recombination prefactor ν :

$$\nu = \frac{AT^2}{N_{DOS}}.$$

A.3 Table A.1

	X_σ [nm]	N_+[m^{-3}]	N_-[m^{-3}]	γ [(m/V)$^{1/2}$]
solid positive branch	5.5	5e25	2e25	8e-4
solid negative branch	4	5e25	5e25	8e-4
dashed positive branch	5	5e25	5e25	5.4e-4
dashed negative branch	5	5e25	5e25	5.4e-4

Table A.1: Table showing the choice of charge distribution used for describing the bandbending of the curves shown in figure 6.7.

A.4 Effect of $\mu(0)$ and γ on IV and ZV curves

Figure A.1 shows the effect of the mobility field-dependency prefactor γ on the calculated IV and ZV curves, for $\mu(0)$ = 5e-11 m^2/Vs, N_{DOS} = 1e27 m^{-3} and $\phi_S = \phi_T$= 0.5 eV. Figure A.2 and A.3 show the effect of the zero-field mobility $\mu(0)$ on the calculated IV and ZV curves for γ = 5.4e-4 (m/V)$^{1/2}$ and γ = 0 (m/V)$^{1/2}$ respectively, using $\phi_S = \phi_T$= 0.5 eV (grey lines) and $\phi_S = \phi_T$= 0.2 eV (black lines). For the IV curves with $\phi_S = \phi_T$ = 0.2 eV, integration of the field was done starting at the injecting contact, because of the unphysically large tunneling distance at low currents, which would be up to 20 nm in this case. A large tunneling distance decreases the distance over which bulk conduction takes place, and thus effectively leads to lower voltages at low currents. The IV curves in figure A.3 show the expected quadratic behaviour of the trap-free square law. The deviation at lower currents to higher voltages for $\phi_S = \phi_T$= 0.5 eV is caused by the fact that the field at the injecting contact is not zero, in which case the trap-free square law does not apply.

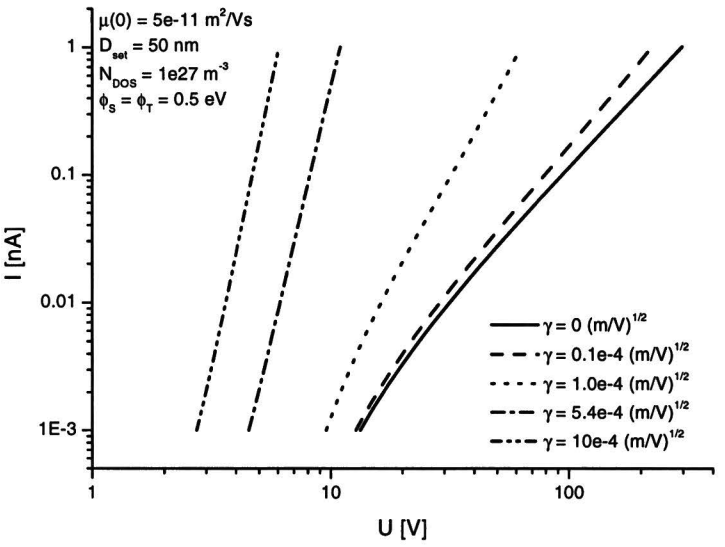

(A)

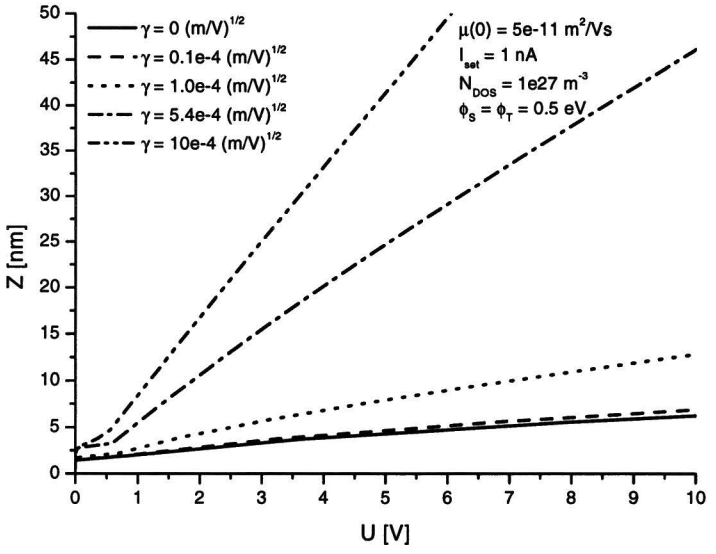

(B)

Figure A.1: Effect of γ on the calculated IV and ZV curves for $\mu(0)$ = 5e-11 m^2/Vs, N_{DOS} = 1e27 m^{-3} and $\phi_S = \phi_T$= 0.5 eV.

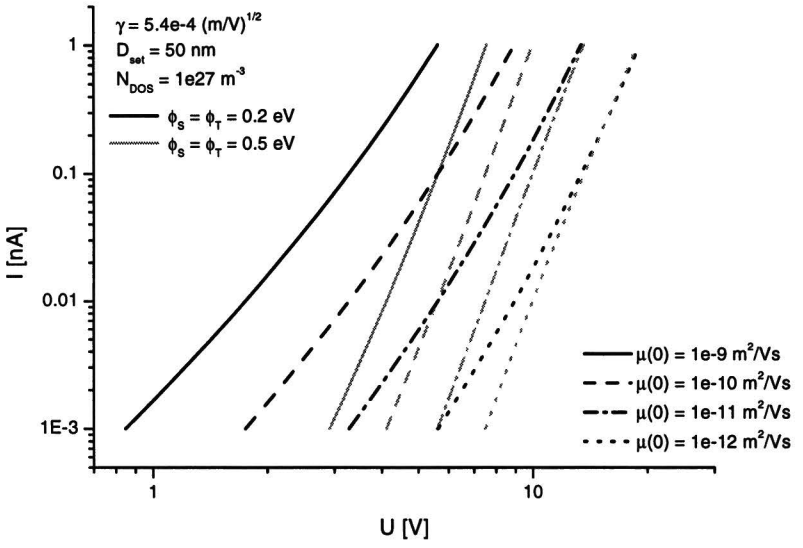

(A)

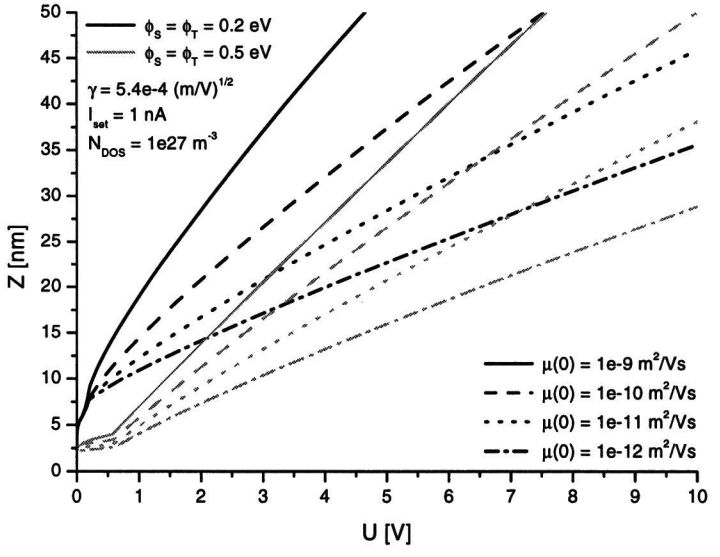

(B)

Figure A.2: Effect of $\mu(0)$ on the calculated IV and ZV curves for γ = 5.4e-4 $(\mathrm{m/V})^{1/2}$, N_{DOS} = 1e27 m^{-3}. For the IV curves with $\phi_S = \phi_T = 0.2$ eV, integration of the field was done starting at the injecting contact, because of the unphysically large tunneling distance at low currents.

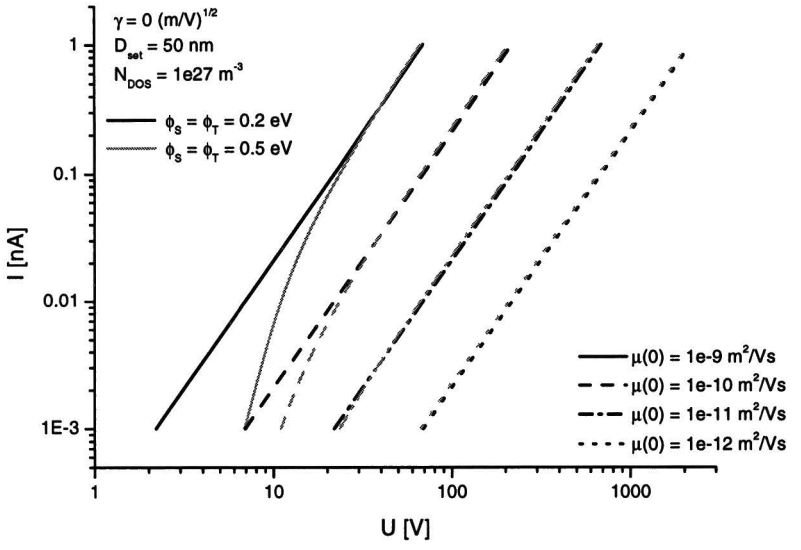

(A)

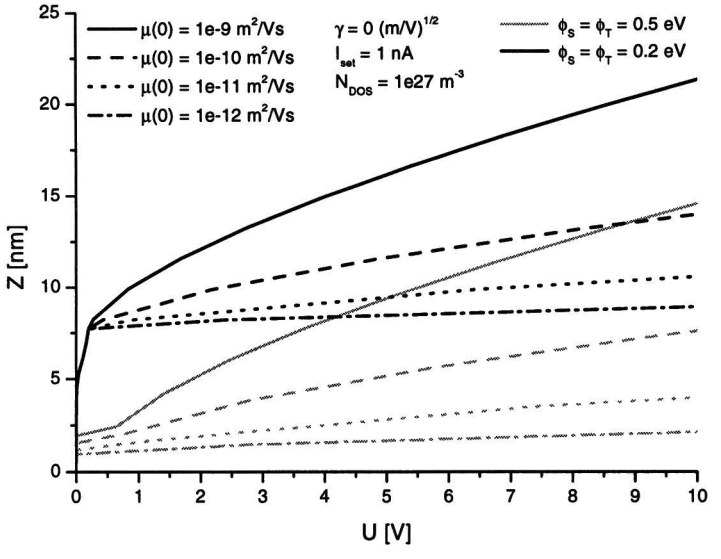

(B)

Figure A.3: Effect of $\mu(0)$ on the calculated IV and ZV curves for $\gamma = 0$ $(\mathrm{m/V})^{1/2}$, $N_{DOS} = 1\mathrm{e}27$ m^{-3}. For the IV curves with $\phi_S = \phi_T = 0.2$ eV, integration of the field was done starting at the injecting contact, because of the unphysically large tunneling distance at low currents.

Bibliography

[1] Private communication with Jeroen van Duren.

[2] Private communication with Peter Bobbert.

[3] L. S. Swanson J. Shinar A. R. Brown D. D. C. Bradley R. H. Friend P. L Burn A. Kraft A. B. Holmes. Electroluminescence-detected magnetic-resonance study of polyparaphenylenevinylene(ppv)-based light-emitting diodes. *Phys. Rev. B*, 46(23):15072, 1992.

[4] A. J. Cambell D. D. C. Bradley D. G. Lidzey. Space-charge limited conduction with traps in poly(phenylene vinylene) light emitting diodes. *J. Appl. Phys.*, 82(12):6326, 1997.

[5] A. J. Campbell M. S. Weaver D. G. Lidzey D. D. C. Bradley. Bulk limited conduction in electroluminescent polymer devices. *J. Appl. Phys.*, 84(12):6737, 1998.

[6] E. Ettedgui H. Razafitrimo Y. Gao B. R. Hsieh. Band bending modified tunneling at metal/conjugated polymer interfaces. *Appl. Phys. Lett.*, 67(18):2705, 1995.

[7] C. Julian Chen. *Introduction to scanning tunneling microscopy.* Oxford university press, Oxford, 1993.

[8] D. H. Dunlap P. E. Parris V. M. Kenkre. Charge-dipole model for the universal field dependence of mobilities in molecularly doped polymers. *Phys. Rev. Lett.*, 77(3):542, 1996.

[9] K. Fesser A. R. Bishop D. K. Campbell. Optical absorption from polarons in a model of polyacetylene. *Phys. Rev. B*, 27(8):4804, 1983.

[10] P. S. Davids A. Saxena D. L. Smith. Nondegenerate continuum model for polymer light-emitting diodes. *J. Appl. Phys.*, 78(6):4244, 1995.

[11] H. Sirringhaus P. J. Brown R. H. Friend M. M. Nielsen K. Bechgaard B. M. W. Langeveld-Voss A. J. H. Spiering R. A. J. Janssen E. W. Meijer P. Herwig D. M. de Leeuw. Two-dimensional charge transport in self-organized, high mobility conjugated polymers. *Nature*, 401:685, 1999.

[12] P. S. Davids Sh. M. Kogan I. D. Parker D.L. Smith. Charge injection in organic light-emitting diodes: Tunneling into low mobility materials. *Appl. Phys. Lett.*, 69(15):2270, 1996.

[13] G. G. Malliaras J. C. Scott. The roles of injection and mobility in organic light emitting diodes. *J. Appl. Phys.*, 83(10):5399, 1998.

[14] H. C. F. Martens P. W. M. Blom H. F. M. Schoo. Comparative study of hole transport in poly(p-phenylene vinylene) derivates. *Phys. Rev. B*, 61(11):7489, 2000.

[15] José A. Freire M. G. E. da Luz Dongge Ma I. A. Huemmelgen. The current-voltage dependance of nominally undoped thin conjugated polymer films. *Appl. Phys. Lett.*, 77(5):693, 2000.

[16] I. D. W. Samuel J. M. Lupton. Temperature-dependant single carrier device model for polymeric light emitting diodes. *J. Phys. D: Appl. Phys.*, 32:2973–2984, 1999.

[17] J. M. Lupton I. D. W. Samuel. Temperature-dependent device model for polymer light-emitting diodes: significance of barrier height. *Synth. Metals*, 111-112:381–384, 2000.

[18] D. Wang J. Shen. A theoretical model for carrier transport in disorderd organic materials. *Synth. Metals*, 111-112:349–351, 2000.

[19] J.-M. Gilles L. Libioulle, Y. Houbion. Very sharp platinum tips for scanning tunneling microscopy. *Rev. Sci. Instrum.*, 66(1):97, 1995.

[20] M. Koehler I.A. Huemmelgen. Temperature dependent tunneling current at metal/polymer interfaces - potential barrier height determination. *Appl. Phys. Lett.*, 70(24):3264, 1997.

[21] P. Mark M.A. Lampert. *Current injection in solids.* Academic Press, London, 1970.

[22] R. H. Friend D. D. C. Bradley P. D. Townsend. Photo-excitation in conjugated polymers. *J. Phys. D.*, 20:1367, 1987.

[23] P. S. Davids I. H. Campbell D. L. Smith. Device model for single carrier organic diodes. *J. Appl. Phys.*, 82(12):6319, 1997.

[24] P. W. M. Blom M. C. J. M. Vissenberg. Dispersive hole transport in poly(p-phenylene vinylene. *Phys. Rev. Lett.*, 80(17):3819, 1998.

[25] P. W. M. Blom M. J. M. de Jong J. J. M. Vleggaar. Electron and hole transport in poly(p-phenylene vinylene) devices. *Appl. Phys. Lett.*, 68(23):3308, 1996.

[26] P. W. M. Blom M. J. M. de Jong M. G. van Munster. Electric-field and temperature dependence of the hole mobility in poly(p-phenylene vinylene). *Phys. Rev. B*, 55(2):r656, 1997.

[27] I. D. Parker. Carrier tunneling and device characteristics in polymer light-emitting diodes. *J. Appl. Phys.*, 75(3):1656, 1994.

[28] Joseph A. Stroscio R. M. Feenstra. Tunneling spectroscopy of the gaas(110) surface. *J. Vac. Sci. Technol. B.*, 5(4):923, 1987.

[29] J.L. Brédas R.R. Chance R. Silbey. Comparative theoretical study of the doping of conjugated polymers: Polarons in polyacetylene and poleparaphenylene. *Phys. Rev. B*, 26(10):5843, 1982.

[30] S. F. Alavarado P. F. Seidler D. G. Lidzey D. D. C. Bradley. Direct determination of the exciton binding energy of conjugatd polymers using a scanning tunneling microscope. *Phys. Rev. Lett.*, 81(5):1082, 1998.

[31] John G. Simmons. Generalized formula for the electric tunnel effect between similar electrodes separated by a thin insulating film. *J. Appl. Phys.*, 34(6):1793, 1963.

[32] S. M. Sze. *Physics of semiconductor devices.* Wiley-InterScience, Chichester, 1981.